

An Abstract of the Thesis of

Alexander Füssel for the degree of Master of Science in
Physics presented on July 14, 1993.

Title: Chemical Phases in the Y-Ba-Cu-O System Identified by TDPAC

Redacted for Privacy

Abstract approved: _____
John A. Gardner

A four detector time differential perturbed angular correlation (PAC) spectrometer has been used to investigate the behavior of the high temperature superconductor $\text{YBa}_2\text{Cu}_3\text{O}_{7-x}$ in the high temperature region between room temperature and 1200°C .

PAC is a hyperfine method, similar to the Mössbauer method, which is very sensitive and can probe very locally.

In this work PAC data were taken of $\text{YBa}_2\text{Cu}_3\text{O}_{7-x}$ in flowing air as well as in flowing oxygen.

The orthorhombic-tetragonal phase transition could be observed at 620°C for flowing air and at 680°C for flowing oxygen.

The decomposition temperature of $\text{YBa}_2\text{Cu}_3\text{O}_{7-x}$ occurred in flowing air at 900°C and in flowing oxygen at 1000°C .

Above the decomposition temperature a new phase could be observed which has previously been interpreted as ^{111}In substituted in a copper site in $\text{YBa}_2\text{Cu}_3\text{O}_{7-x}$ but has now been identified as $\text{Y}_2\text{Cu}_2\text{O}_5$.

The linewidth measured by PAC for the site in $\text{YBa}_2\text{Cu}_3\text{O}_{7-x}$ has no anomalies due to dynamic relaxation anywhere in the temperature range measured.

Chemical Phases in the Y-Ba-Cu-O System Identified by TDPAC

by

Alexander Füssel

A Thesis
submitted to
Oregon State University

in partial fulfillment of
the requirements for the degree of

Master of Science

Completed July 14, 1993
Commencement June 1994

Approved:

Redacted for Privacy

Professor of Physics in charge of major

Redacted for Privacy

Chairman of the Department of Physics

Redacted for Privacy

Dean of Graduate School

Date thesis is presented _____ July 14, 1993

Typed by Alexander Füssel for _____ Alexander Füssel

Table of Contents

1. Introduction	1
1.1 The superconductor $\text{YBa}_2\text{Cu}_3\text{O}_{7-x}$	1
2 Sample preparation	7
2.1 The sol-gel method for $\text{YBa}_2\text{Cu}_3\text{O}_{7-x}$ powder samples	7
2.2 The nitrate evaporation method for $\text{Y}_2\text{Cu}_2\text{O}_5$ samples	11
3. The Theory of $\gamma\gamma$ -perturbed angular correlation (PAC)	13
3.1 General theory of unperturbed angular correlation	13
3.2 Theory of perturbed angular correlation	15
3.3 The static perturbation in polycrystalline material	17
3.4 The static electric quadrupole interaction	19
3.5 The a - b fluctuation model	27
4. Experimental PAC setup	32
4.1 Coincidence electronics	32
4.2 Data analysis and evaluation	34
4.3 Fitted and derived PAC parameters	37
4.4 The effective anisotropy A_{eff} of ^{111}Cd	39
4.5 Probe nuclei for PAC spectroscopy	39
4.6 Accuracy of the temperature measurements	42
5 Overview of PAC measurements on $\text{YBa}_2\text{Cu}_3\text{O}_{7-x}$ and related compounds	43
5.1 PAC measurements on $\text{YBa}_2\text{Cu}_3\text{O}_{7-x}$ from the literature	43
5.2 PAC measurements on $\text{YBa}_2\text{Cu}_3\text{O}_{7-x}$ related compounds from the literature	45
5.3 Calculation of the electric field gradient EFG for $\text{YBa}_2\text{Cu}_3\text{O}_{7-x}$ and related components	47
5.4 The lattice position of ^{111}In in $\text{YBa}_2\text{Cu}_3\text{O}_{7-x}$	56

6. Experimental results of the PAC measurements on $\text{YBa}_2\text{Cu}_3\text{O}_{7-x}$ and $\text{Y}_2\text{Cu}_2\text{O}_5$	
6.1 PAC data on $\text{YBa}_2\text{Cu}_3\text{O}_{7-x}$ in flowing oxygen	57
6.2 PAC data on $\text{YBa}_2\text{Cu}_3\text{O}_{7-x}$ in flowing air	61
6.3 Phase diagram of $\text{YBa}_2\text{Cu}_3\text{O}_{7-x}$	64
6.4 PAC data on $\text{Y}_2\text{Cu}_2\text{O}_5$ in flowing air	67
6.5 The fitting of the observed PAC frequencies	70
7. Discussion and conclusions	72
7.1 Phase stability of $\text{YBa}_2\text{Cu}_3\text{O}_{7-x}$ and second phases	72
7.2 Orthorhombic-tetragonal phase transition	75
7.3 The inapplicability of the a - b fluctuation model	77
7.4 The new phase above decomposition temperature $\text{Y}_2\text{Cu}_2\text{O}_5$ and $\text{Y}_2\text{Ba}_1\text{Cu}_1\text{O}_5$	79
7.5 Summary	80
8. References	81

List of Figures

<u>Figure</u>		<u>Page</u>
1.1	a.) Crystal structure of $\text{YBa}_2\text{Cu}_3\text{O}_7$ and b.) $\text{YBa}_2\text{Cu}_3\text{O}_6$	2
1.2	Neutron diffraction measurement on $\text{YBa}_2\text{Cu}_3\text{O}_{7-x}$ a.) the change in T_c vs. oxygen content b.) the change of the Cu2-O1 bond length vs. oxygen content [3]	3
1.3	The lattice constants of $\text{YBa}_2\text{Cu}_3\text{O}_{7-x}$ for various oxygen partial pressures, the orthorhombic-tetragonal transition temperature decreases with decreasing oxygen pressure [5]	4
1.4	The oxygen content in $\text{YBa}_2\text{Cu}_3\text{O}_{7-x}$ vs. the temperature for different oxygen pressure [6]	5
2.1	X-ray diffraction pattern of a typical $\text{YBa}_2\text{Cu}_3\text{O}_{7-x}$ powder sample, with an oxygen content of $x = 0.2$	9
2.2	AC susceptibility curve of a typical polycrystalline $\text{YBa}_2\text{Cu}_3\text{O}_{7-x}$ powder sample	10
2.3	X-ray diffraction pattern of a typical $\text{Y}_2\text{Cu}_2\text{O}_5$ powder sample	12
3.1	Principle sketch of the PAC theory	13
3.2	The electric quadrupole splitting for a nuclear spin with $I = 5/2$	24
3.3	a.) Eigenvalues and b.) PAC frequencies of the HQ as a function of η for $I = 5/2$	26
3.4	The influence of the fluctuation rate w on G_Q	29
3.5	The theoretical Fourier transform for $\text{YBa}_2\text{Cu}_3\text{O}_{7-x}$ depending on the fluctuation rate	30
4.1	Functional block diagram of the PAC spectrometer	33
4.2	The experimental $A_2G_2(t)$, b.) is computed from the background corrected coincident counts for a 90° and 180° detector pair which is illustrated in a.), c.) the Fourier transform of b.) is performed to obtain a rough estimation of the PAC frequencies and number of possible sites	36
4.3	The ^{111}In to ^{111}Cd decay in a schematic diagram	40

5.1	a.) The calculated electric field gradient and b.) the asymmetry parameter η for ^{111}Cd in $\text{YBa}_2\text{Cu}_3\text{O}_{7-x}$ on a Y-site	51
5.2	a.) The calculated electric field gradient and b.) the asymmetry parameter η for ^{111}Cd in $\text{YBa}_2\text{Cu}_3\text{O}_{7-x}$ on a Cu1-site	52
5.3	a.) The calculated electric field gradient and b.) the asymmetry parameter η for ^{111}Cd in $\text{YBa}_2\text{Cu}_3\text{O}_{7-x}$ on a Cu2-site	53
5.4	a.) The calculated electric field gradient and b.) the asymmetry parameter η for ^{111}Cd in $\text{Y}_2\text{Cu}_2\text{O}_5$ on a Y-site	54
5.5	a.) The calculated electric field gradient and b.) the asymmetry parameter η for ^{111}Cd in $\text{Y}_2\text{Cu}_2\text{O}_5$ on a Cu1-site	55
6.1	The Fourier transform of the time spectra obtained by PAC on $\text{YBa}_2\text{Cu}_3\text{O}_{7-x}$ for various temperatures in flowing oxygen	59
6.2	The Fourier transform of the time spectra obtained by PAC on $\text{YBa}_2\text{Cu}_3\text{O}_{7-x}$ for various temperatures in flowing air	62
6.3	The triangular phase diagrams of $\text{YBa}_2\text{Cu}_3\text{O}_{7-x}$ for various temperatures	66
6.4	The Fourier transform of the time spectra obtained by PAC on $\text{Y}_2\text{Cu}_2\text{O}_5$ in flowing air for various temperatures	68
6.5	The full line width for flowing oxygen on the left side and for flowing air on the right side	71
7.1	The fraction of all observed phases 1-2-3, 2-1-1, 2-0-2 and liquid phase vs. the temperature for a.) flowing oxygen and b.) for flowing air	73
7.2	The asymmetry parameter η and the frequency ω_1 vs. the temperature for $\text{YBa}_2\text{Cu}_3\text{O}_{7-x}$ in flowing oxygen a.) and b.) in flowing air	76
7.3	The frequency ν_Q and the asymmetry parameter η for $\text{YBa}_2\text{Cu}_3\text{O}_{7-x}$ in flowing air after quenching the sample to room temperature.	78

List of Tables

<u>Table</u>		<u>Page</u>
5.1	The PAC parameters of ^{111}Cd in $\text{YBa}_2\text{Cu}_3\text{O}_{7-x}$ measured at RT by other groups and their interpretations	44
5.2	A summary of the PAC investigations done by several groups on compounds that could be formed as minority phases	46
7.1	The observed decomposition temperatures for $\text{YBa}_2\text{Cu}_3\text{O}_{7-x}$ and related compounds	74
7.2	The observed orthorombic-tetragonal phase transition temperature of YBaCuO from the PAC measurement	75

1. Introduction

1.1 The superconductor $\text{YBa}_2\text{Cu}_3\text{O}_{7-x}$

The superconductor $\text{YBa}_2\text{Cu}_3\text{O}_{7-x}$ was discovered in February 1987 by M.K. Wu and C.W. Chu [1] a short time after the discovery of the first superconducting copper oxide ceramic LaBaCuO by J.G. Bednorz and K.A. Mueller [2]. $\text{YBa}_2\text{Cu}_3\text{O}_{7-x}$, often denoted 1-2-3 or YBCO, is a high temperature superconductor with a critical temperature T_c around 92K.

Shortly after the discovery of $\text{YBa}_2\text{Cu}_3\text{O}_{7-x}$, neutron powder diffraction measurements obtained at ILL Grenoble gave more complete information about the oxygen position after x-ray measurements by Bell laboratories gave the cation position [3]. Figure 1.1a. shows that the crystal structure of $\text{YBa}_2\text{Cu}_3\text{O}_7$ is orthorhombic, while the structure for $\text{YBa}_2\text{Cu}_3\text{O}_6$, Fig. 1.1b., is tetragonal. In contrast to metallic $\text{YBa}_2\text{Cu}_3\text{O}_7$, $\text{YBa}_2\text{Cu}_3\text{O}_6$ is an insulator.

Like all copper oxide ceramic superconductors, 1-2-3 contains planes of copper and oxygen atoms which are sandwiched between layers of the other elements, in this case Y and Ba.

Neutron diffraction measurements on 1-2-3 for various oxygen contents Fig.1.2a-b) were made by R.J.Cava and co-workers [4]. One can observe a direct relation between T_c and the length of Cu2-O1 bonds. With the loss of oxygen from the Cu1-O chains and lower T_c , the Cu1-O1 bond shortens and the Cu2-O1 bond lengthens. It is remarkable how the changes in the Cu2-O1 bond Fig. 1.2b) reveal the changes in T_c , including the famous plateaus at 60 and 90K Fig.1.2a). The lengthening of the Cu2-O bonds implies that electrons are being added to the Cu2-O planes, i.e. that electron holes are being removed, and Cu2-O planes are chemically reduced when oxygen is removed from the chain. This loss of electron-holes is the reason for the drop in T_c , so 1-2-3 is a p-type superconductor, which means its conductivity is due to holes. With this behavior it is concluded that the Cu2-O plane is the superconducting plane.

The measurements from Fig. 1.3 reported by [5] show how the lattice constants depend on temperature as well as oxygen pressure. Thus the oxygen partial pressure during measurement is important.

Finally a measurement obtained by Gallagher et al. [6], Fig. 1.4 gives the oxygen content in 1-2-3 vs temperature for different oxygen pressures.

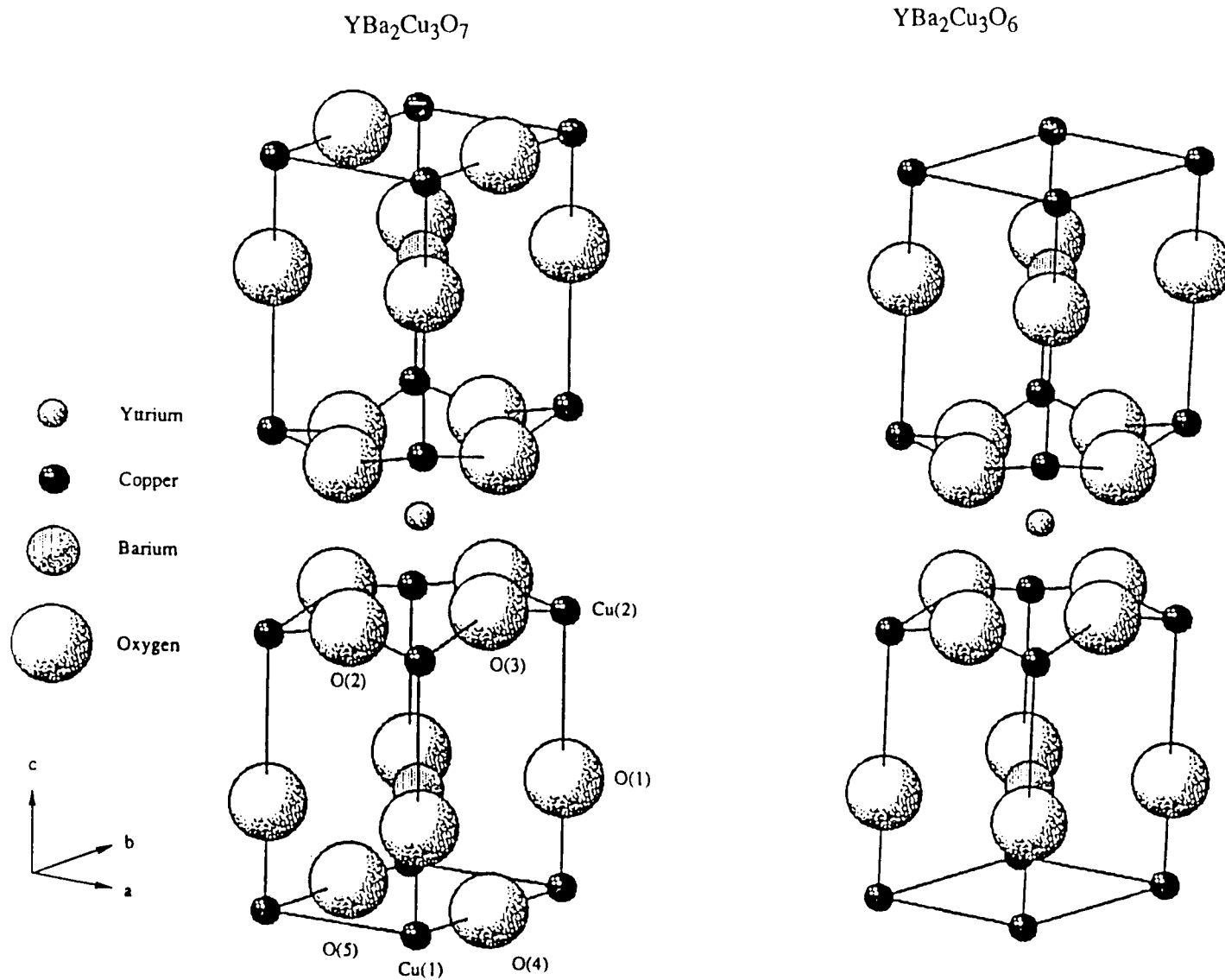


Fig. 1.1.a,b Crystal structure of $\text{YBa}_2\text{Cu}_3\text{O}_7$ and $\text{YBa}_2\text{Cu}_3\text{O}_6$.

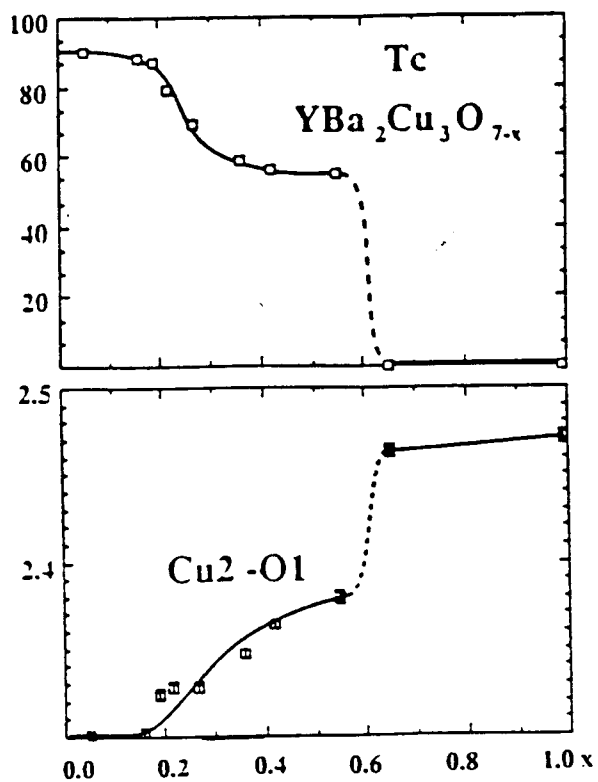


Fig. 1.2.a,b a.) The T_c of $YBa_2Cu_3O_{7-x}$ as a function of x reflected in b.) the changes in the Cu-O1 distance, which implies charge transfer from the Cu2 planes [4].

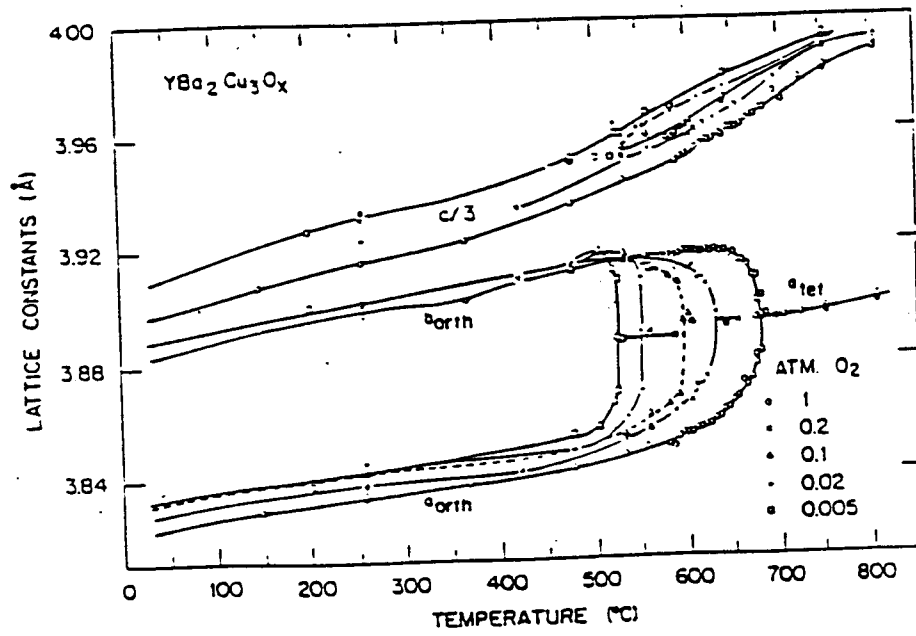


Fig. 1.3. Lattice constants versus temperature for various oxygen partial pressures. The orthorhombic-to-tetragonal transformation temperature decreases with decreasing oxygen pressure [5].

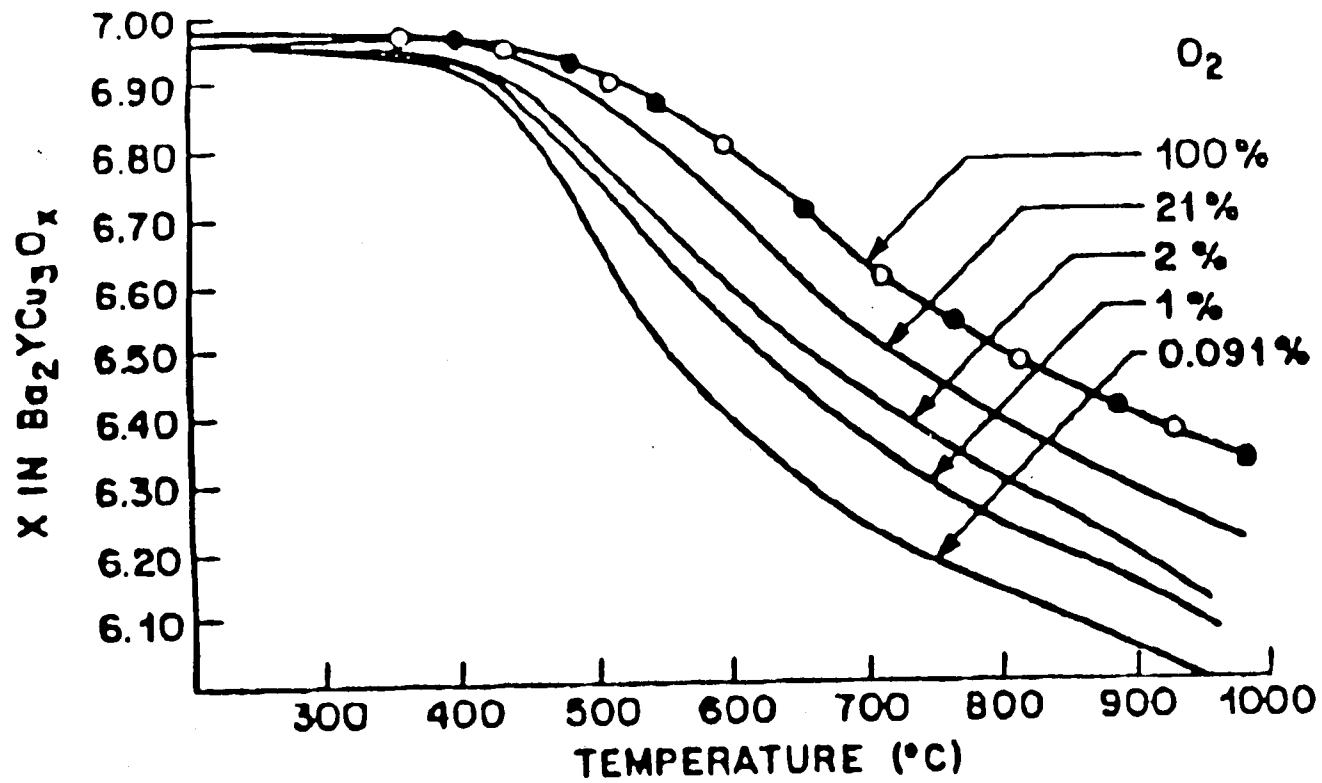


Fig. 1.4 The oxygen content in YBa₂Cu₃O_{7-x} versus the temperature for different oxygen pressure [6].

This behavior gives rise to the question of how the superconductor $\text{YBa}_2\text{Cu}_3\text{O}_{7-x}$ behaves above room temperature, or in other words, how do the oxygen atoms behave from a microscopic point of view. For this reason, in this work perturbed angular correlation (PAC) measurements were done on $\text{YBa}_2\text{Cu}_3\text{O}_{7-x}$ in the high temperature range in order to investigate:

- the microscopic properties measured by PAC near the orthorhombic-tetragonal phase transition for 1-2-3.
- the microscopic properties measured by PAC near the phase stability of 1-2-3 in flowing oxygen as well as in flowing air, and
- to identify the second phases above the decomposition temperature of $\text{YBa}_2\text{Cu}_3\text{O}_{7-x}$.

With the collected PAC parameters one tried also to answer the question whether oxygen motion in the Cu1 plane affects the PAC relaxation.

2. Sample preparation

The PAC method requires the introduction of trace amounts of radioactive isotope into the material to be investigated. Hence, it is very important that the radioactive tracer has some solubility in this material, in this case $\text{YBa}_2\text{Cu}_3\text{O}_{7-x}$. Since it is also crucial that the crystal lattice is not disturbed by the probe material, in this work ^{111}In , experiments were done by G. Weidlich et al. [7] which report that the solubility limit of ^{111}In is 3% per formula unit. Additionally, they did some experiments on $\text{YBa}_2\text{Cu}_3\text{O}_{7-x}$ which suggest that In is most likely substitutional to the Y-site, which will also be discussed in section 2.6.

Dr. James A. Sommers at Teledyne Wah Chang Albany provided the source solutions for the preparation of $\text{YBa}_2\text{Cu}_3\text{O}_{7-x}$ powder samples. The $\text{YBa}_2\text{Cu}_3\text{O}_{7-x}$ samples were prepared by the sol-gel method, while the $\text{Y}_2\text{Cu}_2\text{O}_5$ samples were obtained from the nitrate solution method.

2.1 The sol-gel method for $\text{YBa}_2\text{Cu}_3\text{O}_{7-x}$ powder samples

The following description for the preparation of this solution was given by Dr. Sommers:

From stock nitrate solutions of Y, Ba and Cu, a master solution with cationic molar ratios of 1 : 2 : 3 was made. Crystalline ethylene diamine tetraacetic acid (one mole EDTA for each mole of cations, in accordance with Fransaer, et al. [8] was stirred into this mixture, with little dissolution. Ammonium hydroxide (50 volume percent) was added dropwise until the EDTA dissolved, at pH close to 7. "This kind of a solution had a loading of about 35 mg oxide/ml of solution".

A few drops of a HCl solution containing ^{111}In were added to a few ml of this source material. Afterwards this mixture was evaporated in the way described by Schwenker et al. [9]. The doped solutions were dehydrated and converted to oxides in a ceramic casserole on a hot plate. The solutions evaporated to yield a clear, rigid gel below 100°C . With constant stirring, the gel was further heated to drive

off water, decomposing the nitrate, then oxidizing the organic content. The following sequence was observed: transparent blue gel → blue green crystalline mass evolving nitrogen oxides → fine brown powder with a tendency toward combustion and finally fine black powder. Afterwards this compound was fired in a computer-controlled furnace in the following way:

- Put the powder in at 880°C; keep it there for 1 h,
- in steps of 1°C/min increase to 930°C, and keep it there for 6 h.
- Decrease the temperature to 500°C in steps of 1°C/min, and keep it there for 10 min,
- step down to room temperature at 5°C/min.

In order to check upon the quality of the samples, x-ray and susceptibility measurements were done on non-radioactive material. Figures 2.1 and figure 2.2 show the results of this effort.

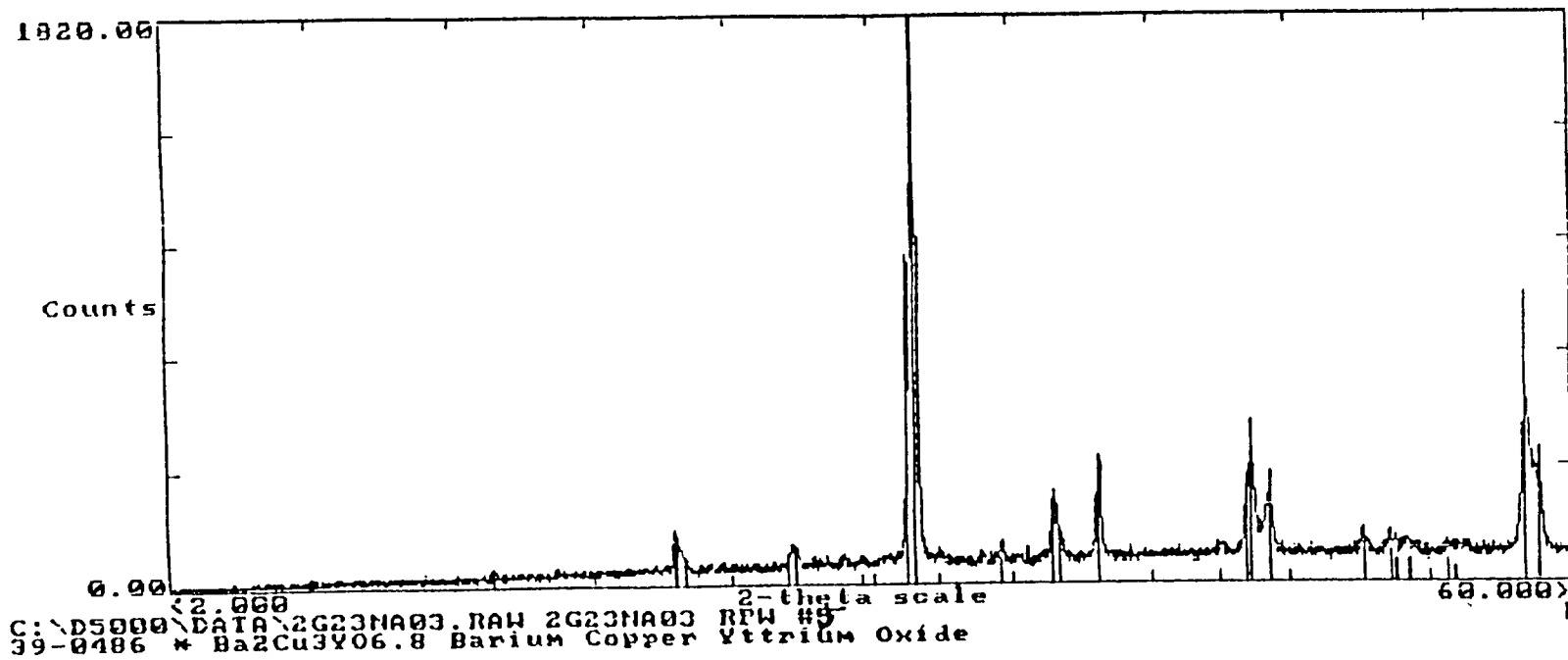


Fig. 2.1 X-ray diffraction pattern of a typical $\text{YBa}_2\text{Cu}_3\text{O}_{7-x}$ powder sample with an oxygen content of $x = 0.2$.

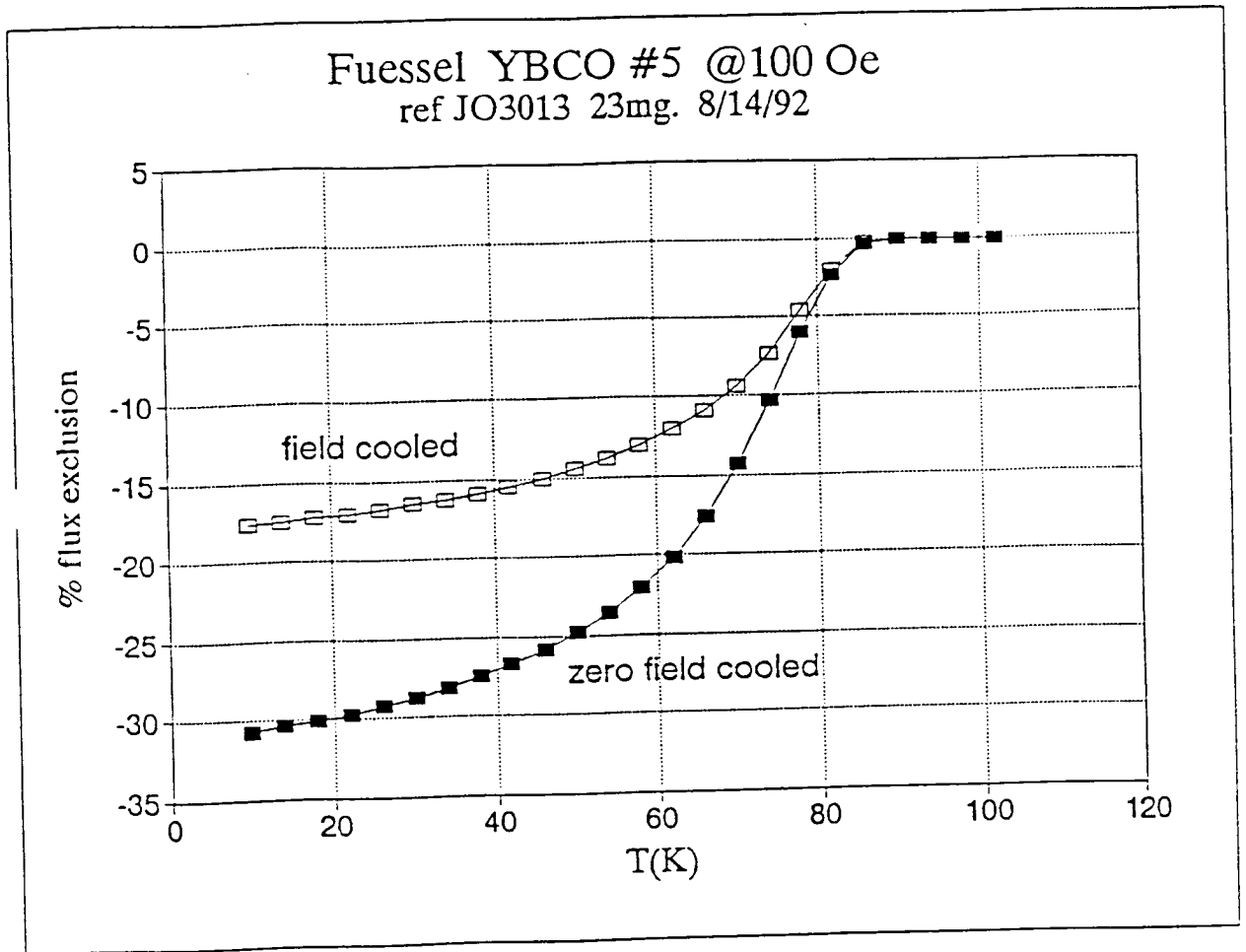


Fig. 2.2 AC susceptibility curve of a typical polycrystalline YBa₂Cu₃O_{7-x} powder sample.

2.2 The nitrate evaporation method for $Y_2Cu_2O_5$ samples

A carefully-prepared nitrate solution with Y:Cu in the molar ratio of 2:2 was used as starting material. A few ml of the solution were taken to which a drop or two of the ^{111}In -containing HCl solution was added. The resulting solution was absorbed into ashless burning wool and then heated in a ceramic casserole and stirred until all liquid had evaporated and the wool carbon had burned off. The nitrate evaporation method allows one to introduce the ^{111}In PAC tracer very uniformly throughout the sample and the wool will keep the components from separating in the evaporation process. Again, the material is much more uniformly mixed than the powders used in the normal solid state synthesis. From here on the same steps outlined in the preceding section were followed. Figure 2.3 shows an x-ray measurement of one of the samples which could be clearly identified as $Y_2Cu_2O_5$.

2-Theta - Scale

04-Jun-1993 16:14

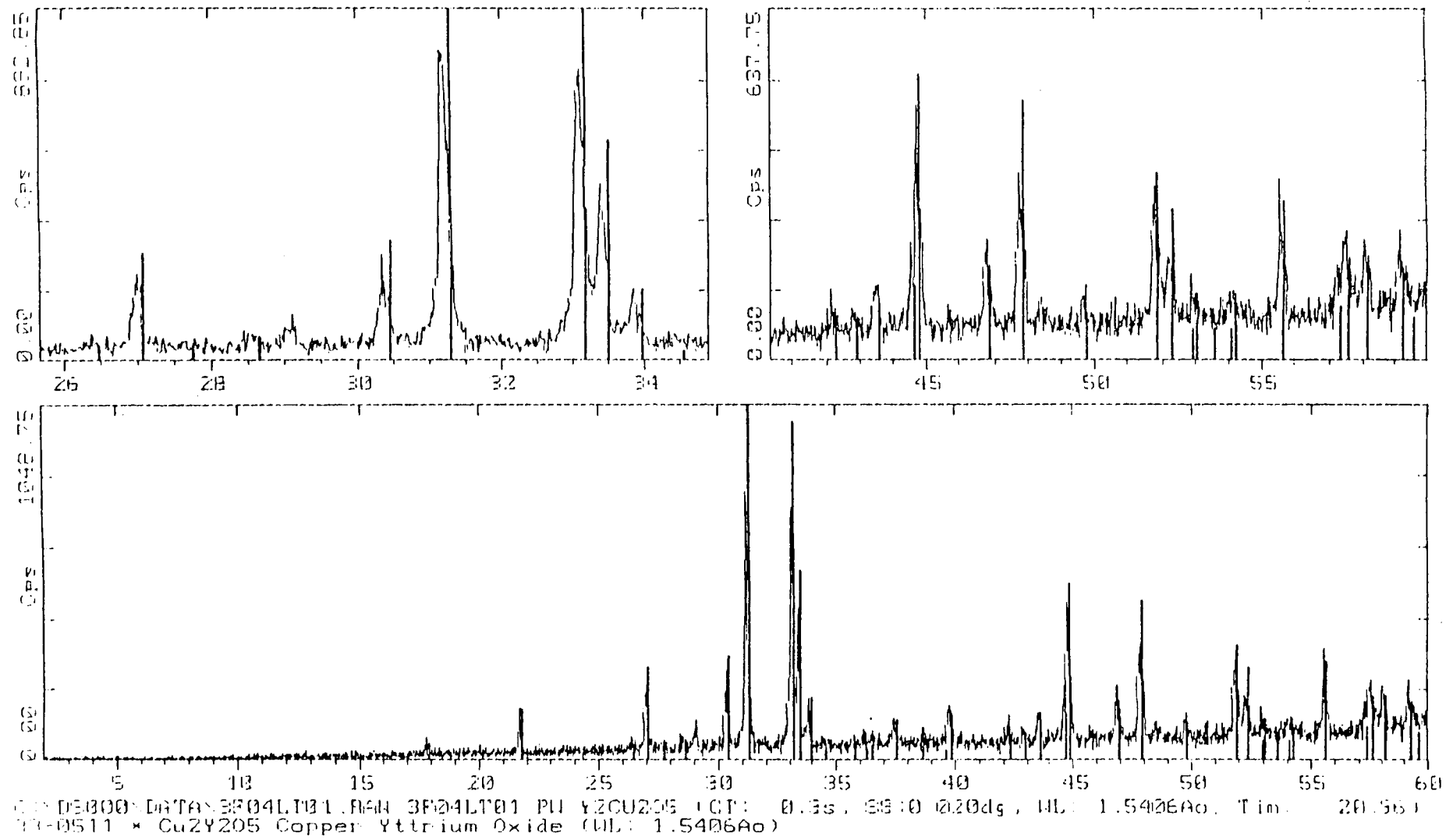


Fig. 2.3 X-ray diffraction pattern of a typical $Y_2Cu_2O_5$ powder sample.

3. The theory of $\gamma\gamma$ -perturbed angular correlation (PAC)

Radiation emitted by atoms or nuclei has a characteristic angular distribution relative to a given axis of quantization. In a macroscopic sample, the nuclei are randomly oriented which results in an isotropic distribution of the emitted radiation.

By the PAC - method which is in some ways similar to the Mössbauer effect, one doesn't measure the energy difference between the γ -rays but the time difference.

Hence a basic supposition is that the radiation distribution of the γ -rays is anisotropic so a sample with oriented nuclei has to be chosen. This can be realized by either subjecting the nuclei to a strong magnetic field or electric field gradient or simply to select from a random ensemble of nuclei only those that are oriented along a given direction. This method requires a nuclear decay that consists of two successive emissions of γ -radiation. The first γ -ray is used to establish a quantization axis against which the second radiation is correlated. This process selects preferentially radiating in the direction of the first detector without the need of orienting the entire ensemble. In this chapter we will discuss the theory of the latter case.

3.1 General theory of unperturbed angular correlation

The principle, which is described in Frauenfelder and Stephen [10], of an angular correlation measurement is shown in figure 3.1.

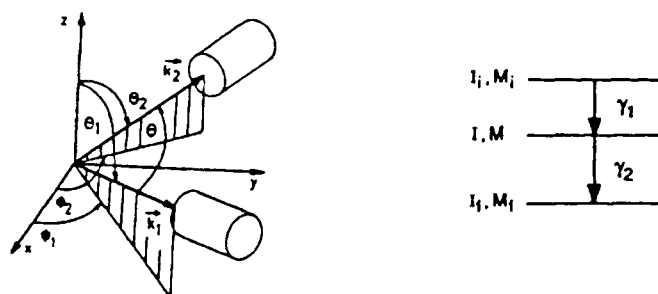


Fig. 3.1 Principle sketch of the PAC theory [11]

We consider a nuclear cascade $I_i \rightarrow I \rightarrow I_f$ with the successive emission of two gamma rays, γ_1 and γ_2 , so the initial state is $|I_i, M_i\rangle$, and this decays to the final state $|I_f, M_f\rangle$ with the emission of γ_2 .

The probability that γ_1, γ_2 are emitted in the directions $\mathbf{k}_1, \mathbf{k}_2$ is given as $W(\mathbf{k}_1, \mathbf{k}_2) d\Omega_1 d\Omega_2$. The function $W(\mathbf{k}_1, \mathbf{k}_2)$ is called the angular correlation function. The most general form of the angular correlation function, using the density matrix formalism is [10]

$$W(\mathbf{k}_1, \mathbf{k}_2, t) = \text{Tr}[\rho(\mathbf{k}_1, t)\rho(\mathbf{k}_2, 0)] = \sum_{mm'} \langle m | \rho(\mathbf{k}_1, t) | m' \rangle \langle m' | \rho(\mathbf{k}_2, 0) | m \rangle, \quad (3-1)$$

where $\rho(\mathbf{k}_1, t)$ and $\rho(\mathbf{k}_2, 0)$ are the density operators describing the system under discussion immediately after the emission of γ_1 and γ_2 . Since we assume here that the nuclei are not subject to external fields, ρ does not depend on time, so we can evaluate ρ at $t = 0$.

$$\langle m | \rho(\mathbf{k}_1, 0) | m' \rangle = \sum_{k_1 N_1} (-1)^{2I_i - I_i + m} A_{k_1(1)} \begin{pmatrix} I & I & k_1 \\ m' & -m & N_1 \end{pmatrix} \sqrt{4\pi} Y_{k_1 N_1}(\theta_1, \phi_1) \quad (3-2)$$

$$\langle m' | \rho(\mathbf{k}_2, 0) | m \rangle = \sum_{k_2 N_2} (-1)^{k_2 - I_f - m} A_{k_2(2)} \begin{pmatrix} I & I & k_2 \\ m' & -m & N_2 \end{pmatrix} \sqrt{4\pi} Y_{k_2 N_2}(\theta_2, \phi_2) \quad (3-3)$$

Now we insert Eq. (3-2) and (3-3) in (3-1) and by using the orthogonality relations for the 3-j symbols we may write

$$W(\mathbf{k}_1, \mathbf{k}_2) = \sum_{kN} (-1)^k A_{k(1)} A_{k(2)} \frac{4\pi}{2k+1} Y_{kN}(\theta_1, \phi_1) Y_{kN}(\theta_2, \phi_2) \quad (3-4)$$

If we sum now over N , we can reduce Eq.(3-4) to

$$W(\mathbf{k}_1, \mathbf{k}_2) = \sum_k (-1)^k A_{k(1)} A_{k(2)} P_k(\cos\theta). \quad (3-5)$$

Since we assume that polarization of the emitted radiation is not observed, $W(\mathbf{k}_1, \mathbf{k}_2)$ simplifies to the directional correlation function $W(\theta)$ with θ the angle between γ_1 and γ_2 .

We also can argue that k has to be even, because otherwise parity is not conserved, and so

$$W(\mathbf{k}_1, \mathbf{k}_2) = W(\theta) = \sum_{k=0 \text{ even}}^{k_{\max}} A_{k(1)} A_{k(2)} P_k(\cos\theta) \quad (3-6)$$

3.2. Theory of perturbed angular correlation

Now we assume that our intermediate state $|I, M\rangle$ has a finite lifetime τ_n . Hence perturbations like external fields can influence the angular correlation function during the lifetime τ_n .

We now write for $W(\mathbf{k}_1, \mathbf{k}_2, t)$

$$W(\mathbf{k}_1, \mathbf{k}_2, t) = \sum_{mm'} \langle m | \rho(\mathbf{k}_1, t) | m' \rangle \langle m' | \rho(\mathbf{k}_2, 0) | m \rangle \quad (3-7)$$

and note that $\rho(\mathbf{k}_1, t)$ depends on time and can hence change.

We define the sublevels of the intermediate state with m_a, m_a', \dots and m_b, m_b', \dots and by introducing the perturbation factor $G(t)$ we can write

$$\langle m | \rho(\mathbf{k}_1, t) | m' \rangle = \sum_{m_b m_b'} \langle m_b | \rho(\mathbf{k}_1, 0) | m_b' \rangle \langle m_b m_b' | G(t) | m_a m_a' \rangle \quad (3-8)$$

With $\rho(\mathbf{k}_1, t) = \Lambda(t) \rho(\mathbf{k}_1, 0) \Lambda^\dagger(t)$ and $\Lambda \equiv$ time evolution operator for the intermediate state of nucleus, we get

$$\langle m_b m_b' | G(t) | m_a m_a' \rangle = \langle m_a | \Lambda(t) | m_b \rangle \langle m_a' | \Lambda(t) | m_b' \rangle^* \quad (3-9)$$

If we insert Eq.(3-8) in Eq.(3-7) and use Eq's. (3-2) and (3-3) we get

$$W(\mathbf{k}_1, \mathbf{k}_2, t) = \sum_{k_1 k_2 N_1 N_2} [(2k_1+1)(2k_2+1)] \frac{-1}{2} A_{k(1)} A_{k(2)} G_{k_1 k_2}^{N_1 N_2}(t) \times Y_{k_1 N_1}^*(\theta_1, \phi_1) Y_{k_2 N_2}(\theta_2, \phi_2), \quad (3-10)$$

where the perturbation factor is defined as

$$G_{k_1 k_2}^{N_1 N_2}(t) = \sum_{m_a m_a' m_b m_b'} (-1)^{2I+m_a+m_b} [(2k_1+1)(2k_2+1)]^{\frac{1}{2}} \begin{pmatrix} I & I & k_1 \\ m_a' & -m_a & N_1 \end{pmatrix} \begin{pmatrix} I & I & k_2 \\ m_b' & -m_b & N_2 \end{pmatrix} \times \langle m_a | \Lambda(t) | m_b \rangle^* \langle m_a' | \Lambda(t) | m_b' \rangle. \quad (3-11)$$

We calculate the perturbation factor by assuming a static, axisymmetric interaction between the nuclei and an external field with the evolution operator $\Lambda(t)$:

$$\Lambda(t) = e^{-iHt/\hbar}.$$

We write

$$\langle m_a | \Lambda(t) | m_b \rangle = \langle m_a | e^{-iHt/\hbar} | m_b \rangle = \sum_n e^{-iE_n t/\hbar} \langle m_a | n \rangle \langle m_b | n \rangle^*, \quad (3-12)$$

where $|n\rangle$ are eigenvectors of H : $H|n\rangle = E_n|n\rangle$.

Now we can write Eq.(3-11) as

$$G_{k_1 k_2}^{N_1 N_2}(t) = \sum_{nn'} \sum_{m_a m_a'} \sum_{m_b m_b'} (-1)^{2I+m_a+m_b} [(2k_1+1)(2k_2+1)]^{\frac{1}{2}} \begin{pmatrix} I & I & k_1 \\ m_a' & -m_a & N_1 \end{pmatrix} \begin{pmatrix} I & I & k_2 \\ m_b' & -m_b & N_2 \end{pmatrix}^* e^{-i/\hbar (E_n - E_{n'}) t} \langle m_a | n \rangle \langle m_a' | n' \rangle^* \langle m_b | n \rangle^* \langle m_b' | n' \rangle. \quad (3-13)$$

so we can reduce Eq. (3-13) to

$$G_{k_1 k_2}^{N_1 N_2}(t) = \sum_{nn'} [(2k_1+1)(2k_2+1)]^{\frac{1}{2}} \begin{pmatrix} I & I & k_1 \\ n' & -n & N \end{pmatrix} \begin{pmatrix} I & I & k_2 \\ n' & -n & N \end{pmatrix} \times e^{-i/\hbar (E_n - E_{n'}) t}. \quad (3-14)$$

by summing over $\sum_{m_a m_a'}$ and $\sum_{m_b m_b'}$ we get that $\langle m_a | n \rangle = \delta_{n, m_a}$, $\langle m_b | n \rangle = \delta_{n, m_b}$

3.3 The static perturbation in polycrystalline material

In this work, the perturbed angular correlation measurements were done on powder samples since it is experimentally much easier to work with polycrystalline samples. A powder consists of a large number of randomly-oriented micro crystals, so it is convenient to reformulate the problem in terms of axes fixed with respect to k_1 and k_2 .

For this reason, we use the rotation matrix $D(\omega)$ to transform the interaction Hamiltonian $H(t)$ from the lab system to the principal axis system z' :

$$H(z') = D(\omega) H(z) D^{-1}(\omega).$$

With U an operator which diagonalizes $H(z')$ we write

$$\Lambda(t) = D^{-1}(\omega) U^{-1} e^{-iE_n t/\hbar} U D(\omega). \quad (3-15)$$

Hence, with terms of type $D^{I m_1 m_a}(\omega) = \langle m_1 | D(\omega) | m_a \rangle \dots$, which are the matrix elements of the rotation operator,

$$\langle m_a | \Lambda(t) | m_b \rangle = \sum_{m_1 m_2 n} e^{-iE_n t/\hbar} D^{I m_1 m_a}(\omega) D^{I m_2 m_b}(\omega) \langle m | m_1 \rangle^* \langle m | m_2 \rangle \quad (3-16)$$

and $\langle m_b m'_b | G(t) | m_a m'_a \rangle$ can now be written as

$$\langle m_b m'_b | G(t) | m_a m'_a \rangle = \sum_{m_1 m_1'} \sum_{m_2 m_2'} \sum_{n n'} \langle m_1 | n \rangle \langle m_1' | n' \rangle \langle m_2 | n \rangle \langle m_2' | n' \rangle \times e^{-i/\hbar (E_n - E_{n'}) t} D^{I^* m_1 m_a}(\omega) D^{I m_1' m_a}(\omega) D^{I m_2 m_b}(\omega) D^{I^* m_2' m_b}(\omega) \quad (3-17)$$

The perturbation factor in Eq.(3-13) becomes then by using the contraction relation for the $3j$ - symbols and summing over all sub levels a, a', b, b' ,

$$G_{k_1 k_2}^{N_1 N_2} = \sum_{m_1 m_1'} \sum_{m_2 m_2'} \sum_{n n'} (-1)^{2I+m_1+m_2} [(2k_1+1)(2k_2+1)]^{\frac{1}{2}} e^{-i/\hbar (E_n - E_{n'}) t} \times \begin{pmatrix} I & I & k_1 \\ m_1' & m_1 & p_1 \end{pmatrix} \begin{pmatrix} I & I & k_2 \\ m_2' & m_2 & p_2 \end{pmatrix} D^{k_1^* p_1 N_a}(\omega) D^{k_2^* p_2 N_b}(\omega) \times \langle m_1 | n \rangle \langle m_1' | n' \rangle^* \langle m_2 | n \rangle^* \langle m_2' | n' \rangle. \quad (3-18)$$

Here we made the substitution $p_1 = m_1 - m'_1$ and $p_2 = m_2 - m'_2$. Since we have many microcrystals which are randomly oriented, we have to average over all orientations in order to take the contribution of the different rotation matrices into account.

$$\int d\omega G_{k_1 k_2}^{N_1 N_2}(t) = \delta_{k_1 k_2} \delta_{N_1 N_2} \sum_{nn'} S_{nn'}^{k_1 k_2} e^{-i/\hbar (E_n - E_{n'}) t}, \quad (3-19)$$

since the orthogonality relation for the rotation matrices is

$$\int d\Omega D_{j_1 m_1 m_a}(\Omega) D_{j_2 m_2 m_2}(\Omega) = \frac{1}{2j_1 + 1} \delta_{j_1 j_2} \delta_{m_1 m_2} \delta_{m_1' m_2'}. \quad (3-20)$$

We defined in Eq.3-18 the coefficient as :

$$S_{nn'}^{k_1 k_2} = \sum_{m_1 m_1'} \sum_{m_2 m_2'} (-1)^{2I+m_1+m_2} \begin{pmatrix} I & I & k_1 \\ m_1' & -m_1 & p \end{pmatrix} \begin{pmatrix} I & I & k_2 \\ m_2' & -m_2 & p \end{pmatrix} \times \\ \langle m_1 | n \rangle^* \langle m_1' | n' \rangle \langle m_2 | n \rangle \langle m_2' | n' \rangle^* \quad (3-21)$$

and the perturbation factor for a polycrystalline sample is now written as

$$G_{kk}(t) = \sum_{m_1 m_1'} \sum_{m_2 m_2'} \sum_{nn'} (-1)^{2I+m_1+m_2} \begin{pmatrix} I & I & k_1 \\ m_1' & -m_1 & p \end{pmatrix} \begin{pmatrix} I & I & k_2 \\ m_2' & -m_2 & p \end{pmatrix} \times \\ e^{-i/\hbar (E(n) - E(n')) t} \langle m_1 | n \rangle \langle m_1' | n' \rangle^* \langle m_2 | n \rangle \langle m_2' | n' \rangle^*. \quad (3-22)$$

If we compare this result for a powder sample with our result from Eq.(3-13), it shows that the perturbation factor for a powder sample is the average of the perturbation factors $G_{kk}^{pp}(t)$ of the single crystal, so we can write

$$G_{kk}(t) = \frac{1}{2k+1} \sum_{p=-k}^k G_{kk}^{pp}(t). \quad (3.23)$$

If we put Eq.(3-21) in Eq.(3-22), we get

$$G_{kk}(t) = \sum_{nn'} S_{nn'}^{k_1 k_2} e^{-i (E_n - E_{n'}) t/\hbar}, \quad (3-24)$$

which can also be written as

$$G_{kk}(t) = \sum_n S_{nn}^{kk} + \sum_{n \neq n'} S_{nn'}^{kk} e^{-i (E_n - E_{n'}) t/\hbar}. \quad (3-25)$$

Since the perturbation function is independent of N_1 and N_2 in Eq.(3-10), the summation over N_1 and N_2 can be done independently, and we still can apply the addition theorem for spherical harmonics, so we finally can write the correlation function for a polycrystalline sample with static interaction as

$$W(\theta, t) = \sum_{k=0 \text{ even}}^{k_{\max}} A_{kk} G_{kk} P_k(\cos\theta). \quad (3-26)$$

An important feature of the perturbation function for the powder sample is the time-independent term $\sum_n S_{nn}^{kk}$. Because of this constant term, the angular

correlation of the polycrystalline sample is never completely destroyed under the influence of the static perturbing fields. For this reason, this term has historically been called the "hard core".

3.4 The static electric quadrupole interaction

In order to work with the angular correlation function, derived above, we need to know the energies E_n . In a solid each nucleus is surrounded by electric charges which produce a potential $\Phi(\mathbf{r})$ at the nucleus [11]. The energy of the charge distribution $\rho(\mathbf{r})$ in this outer potential $\Phi(\mathbf{r})$ is given by

$$E_{\text{elec.}} = \int \rho(\mathbf{r}) \Phi(\mathbf{r}) \, d\mathbf{r}^3, \quad (3-27)$$

with: $\int \rho(\mathbf{r}) \, d\mathbf{r}^3 = Z e.$

In order to calculate E_{elec} we expand the electric potential in a Taylor series around $\mathbf{r} = 0$:

$$\Phi(\mathbf{r}) = \Phi_0 + \sum_{\alpha=1}^3 \left(\frac{\partial \Phi}{\partial x_{\alpha}} \right) x_{\alpha} + \frac{1}{2} \sum_{\alpha=1}^3 \left(\frac{\partial^2 \Phi}{\partial x_{\alpha} \partial x_{\beta}} \right) x_{\alpha} x_{\beta} + \dots \quad (3-28)$$

so we get for the energy:

$$E_{\text{elec.}} = E^{(0)} + E^{(1)} + E^{(2)} + \dots$$

The first term of this expression is just the energy of a point charge which contributes to the potential energy but can be neglected in our case, since it is simply a constant offset.

The second term stands for the electric dipole interaction, but since we require the conservation of parity, this term is zero.

Hence the leading term of importance for us is the third term $E^{(2)}$, which also can be written as

$$E^{(2)} = \frac{1}{2} \sum_{\alpha\beta} \Phi_{\alpha\beta} \int \rho(\mathbf{r}) x_{\alpha} x_{\beta} \, d\mathbf{r}^3, \quad (3-29)$$

$$\Phi_{\alpha\beta} = \left(\frac{\partial^2 \Phi}{\partial x_{\alpha} \partial x_{\beta}} \right),$$

which is a 3×3 symmetric matrix that can be diagonalized to principal axis by an orthogonal transformation.

that $r^2 = x_1^2 + x_2^2 + x_3^2$ and:

$$E^{(2)} = \frac{1}{2} \sum_{\alpha} \Phi_{\alpha\alpha} \int \rho(\mathbf{r}) x_{\alpha}^2 d\mathbf{r}^3 = \frac{1}{6} \sum_{\alpha\alpha} \Phi_{\alpha\alpha} \int \rho(\mathbf{r}) r^2_{\alpha} d\mathbf{r}^3 + \quad (3-30)$$

$$\frac{1}{2} \sum_{\alpha} \Phi_{\alpha\alpha} \int \rho(\mathbf{r}) \left(x_{\alpha}^2 - \frac{r^2}{3} \right) d\mathbf{r}^3 .$$

The electrostatic potential $\Phi(\mathbf{r})$ is given by the Poisson equation at the nucleus

$$\text{with } \Delta\Phi - \sum_{\alpha} \Phi_{\alpha\alpha} = \frac{e}{\epsilon_0} |\psi_0|^2,$$

$$\text{so } E^{(2)} = E_C + E_Q. \quad (3-31)$$

From Eq.(3-30) we see that E_C , the contact term, only depends on the average quadratic radius of the nucleus. This means we get just a shift but no splitting of the sublevels which does not affect our measurements. So the only term left is E_Q :

$$E_Q = \frac{e}{6} \sum_{\alpha} \Phi_{\alpha\alpha} Q_{\alpha\alpha} , \quad (3-32)$$

and the quadrupole moment of the nucleus is

$$Q_{\alpha\alpha} = \frac{1}{e} \int \rho(\mathbf{r}) (3x_{\alpha}^2 - r^2) d\mathbf{r}^3 . \quad (3-33)$$

If we separate

$$\Phi_{\alpha\alpha} = V_{\alpha\alpha} + \frac{1}{3} (\Delta\Phi) \delta_{\alpha\alpha} \quad (3-34)$$

by assuming that $(\Delta\Phi) = \sum \Phi_{\alpha\alpha}$,

our new matrix $V_{\alpha\alpha}$ is trace-free, and by putting Eq. (3-34) in Eq. (3-32) we see that the part with $\frac{1}{3} (\Delta\Phi) \delta_{\alpha\alpha}$ does not contribute to the energy E_Q since

$$\sum_{\alpha} Q_{\alpha\alpha} = 0. \text{ Hence}$$

$$E_Q = \frac{e}{6} \sum_{\alpha} V_{\alpha\alpha} Q_{\alpha\alpha}. \quad (3-35)$$

We call the matrix $V_{\alpha\alpha}$ the tensor of the electric field gradient. Only charges which are not localized at the nucleus contribute to $V_{\alpha\alpha}$. For example, for a spherical charge distribution (s-electrons), we have $V_{xx} = V_{yy} = V_{zz}$, but since $\sum_{\alpha} V_{\alpha\alpha} = 0$, all components of the electric field gradient have to be zero and do

not affect E_Q . Since $\sum_{\alpha} V_{\alpha\alpha} = 0$, we can define the electric field gradient totally

by two parameters. By ideal choice of the principal axes we can have that $|V_{xx}| \leq |V_{yy}| \leq |V_{zz}|$. Then as parameters one conventionally chooses V_{zz} and the asymmetry parameter η which is defined by

$$\eta = \frac{V_{xx} - V_{yy}}{V_{zz}}. \quad (3-36)$$

In order to calculate the energy E_Q , it is easier to express the nuclear quadrupole moment and the electric field gradient by spherical tensors.

The tensor components for the electric field gradient are

$$V_{20} = \frac{1}{4} \sqrt{\frac{5}{\pi}} V_{zz}, \quad (3-37a)$$

$$V_{2\pm 1} = \pm \frac{1}{2} \sqrt{\frac{5}{6\pi}} (V_{xz} \pm V_{yz}), \quad (3-37b)$$

$$V_{2\pm 2} = \frac{1}{4} \sqrt{\frac{5}{6\pi}} (V_{xx} - V_{yy} \pm 2iV_{xy}). \quad (3-37c)$$

If we carry out a principal axis transformation, then

$$V_{20} = \frac{1}{4} \sqrt{\frac{5}{\pi}} V_{zz}, \quad V_{2\pm 1} = 0,$$

$$V_{2\pm 2} = \frac{1}{4} \sqrt{\frac{5}{6\pi}} (V_{xx} - V_{yy}) = \frac{1}{4} \sqrt{\frac{5}{6\pi}} \eta V_{zz}.$$

In classical physics the electric quadrupole moment is written as

$$Q = \frac{1}{e} \sqrt{\frac{16\pi}{5}} \int \rho(r) r^2 Y_2^0 dr^3, \quad (3-38)$$

while in quantum mechanics we define Q as the expectation value of the quadrupole operators

$$Q = \sqrt{\frac{16\pi}{5}} \langle I, M=I | r^2 Y_2^0 | I, M=I \rangle, \quad (3-39)$$

with Y_2^0 = the spherical harmonics. Hence,

$$\langle I, M | Q_{20} | I, M \rangle = (-1)^{I-M} \begin{pmatrix} I & 2 & I \\ -M & 0 & M \end{pmatrix} \langle I | Q_2 | I \rangle \quad (3-40)$$

by the Wigner-Eckart Theorem.

Hence, we can define the tensor of the electric quadrupole moment of the nucleus as

$$Q_{2q} = r^2 Y_2^q.$$

So we have for the quadrupole energy

$$E_Q = \frac{4\pi}{5} \sum_q (-1)^q e Q_{2q} V_{2-q}. \quad (3-41)$$

We want to consider only the axially symmetric case where $V_{xx} = V_{yy} \rightarrow \eta = 0$.

$$\text{In this case,} \quad E_Q = \frac{\pi}{5} e Q_{20} V_{zz}. \quad (3-42)$$

But from quantum mechanics we know that

$$E_Q = \frac{\pi}{5} e V_{zz} \langle I, M | Q_{20} | I, M \rangle, \quad (3-43)$$

with $\langle I, M | Q_{20} | I, M \rangle$ given in Eq. (3-40). Since Eq. (3-39) is a definition, we combine Eq. (3-39) and Eq. (3-40) and put them in Eq. (3-43), resulting in

$$E_Q = \frac{1}{4} V_{zz} (-1)^{I-M} \frac{\begin{pmatrix} I & 2 & I \\ -M & 0 & M \end{pmatrix}}{\begin{pmatrix} I & 2 & I \\ I & 0 & I \end{pmatrix}} e Q, \quad (3-44)$$

Then

$$E_Q = \frac{3M^2 - I(I+1)}{4I(2I-1)} e Q V_{zz} \quad (3-45)$$

and the transition energy between two sublevels M and M' can be written as

$$E_{Q(M)} - E_{Q(M')} = \frac{e Q V_{zz}}{4I(2I-1)} = 3(M^2 - M'^2) \hbar \omega_Q \quad (3-46)$$

where we define the quadrupole frequency by $\omega_Q = \frac{e Q V_{zz}}{4I(2I-1)\hbar}$.

Because $|M^2 - M'^2| = (M + M')(M - M')$, the number is always integral. The lowest transition frequencies are

$$\begin{aligned} \omega_{Q^0} &= 6 \omega_Q && \text{for half integer nuclear spin } I, \\ \omega_{Q^0} &= 3 \omega_Q && \text{" integer " } \end{aligned}$$

In the literature it is more common to use the quadrupole-coupling constant ν_Q since it has no dependence on the angular momentum:

$$\nu_Q = \frac{e Q V_{zz}}{h} \quad (3-47)$$

An example of the electric quadrupole splitting for a nuclear spin with $I = 5/2$ is given in figure 3.2.

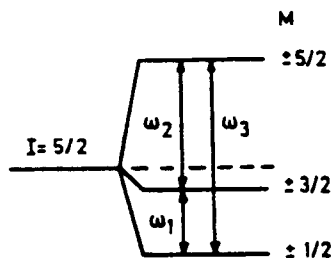


Fig. 3.2 The electric quadrupole splitting for a nuclear spin with $I = 5/2$.

$$E_{Q(M=\pm 1/2)} = -\frac{1}{5} e Q V_{zz},$$

$$E_{Q(M=\pm 3/2)} = -\frac{1}{20} e Q V_{zz},$$

$$E_{Q(M=\pm 5/2)} = \frac{1}{4} e Q V_{zz}.$$

So the transition frequencies are

$$\omega_1 = \omega_{Q^0} = \frac{E_q(\pm 3/2) - E_q(\pm 1/2)}{\hbar} = \frac{3 e Q V_{zz}}{20 \hbar} = 6\omega_Q,$$

$$\omega_2 = \frac{E_q(\pm 5/2) - E_q(\pm 3/2)}{\hbar} = \frac{6 e Q V_{zz}}{20 \hbar} = 12\omega_Q,$$

$$\omega_3 = \omega_1 + \omega_2 = \frac{9 e Q V_{zz}}{20 \hbar} = 18\omega_Q.$$

Until now we have considered the axially symmetric field gradient with $\eta = 0$.

Now we want to think about the cases where η is not zero, here the calculation of the matrix elements for E_Q is rather difficult since most of the time the Hamiltonian has to be diagonalized numerically.

The interaction Hamiltonian for ^{111}Cd with a nuclear spin of $I = 5/2$ at the intermediate state is

$$H_Q = \hbar\omega_Q \begin{bmatrix} 10 & 0 & \eta\sqrt{10} & 0 & 0 & 0 \\ 0 & -2 & 0 & 3\eta\sqrt{2} & 0 & 0 \\ \eta\sqrt{10} & 0 & -8 & 0 & 3\eta\sqrt{2} & 0 \\ 0 & 3\eta\sqrt{2} & 0 & -8 & 0 & \eta\sqrt{10} \\ 0 & 0 & 3\eta\sqrt{2} & 0 & -2 & 0 \\ 0 & 0 & 0 & \eta\sqrt{10} & 0 & 10 \end{bmatrix}$$

Figure 3.3 shows a.) the eigenvalues and b.) PAC frequencies of the H_Q as a function of η for $I = 5/2$ with fixed V_{zz} .

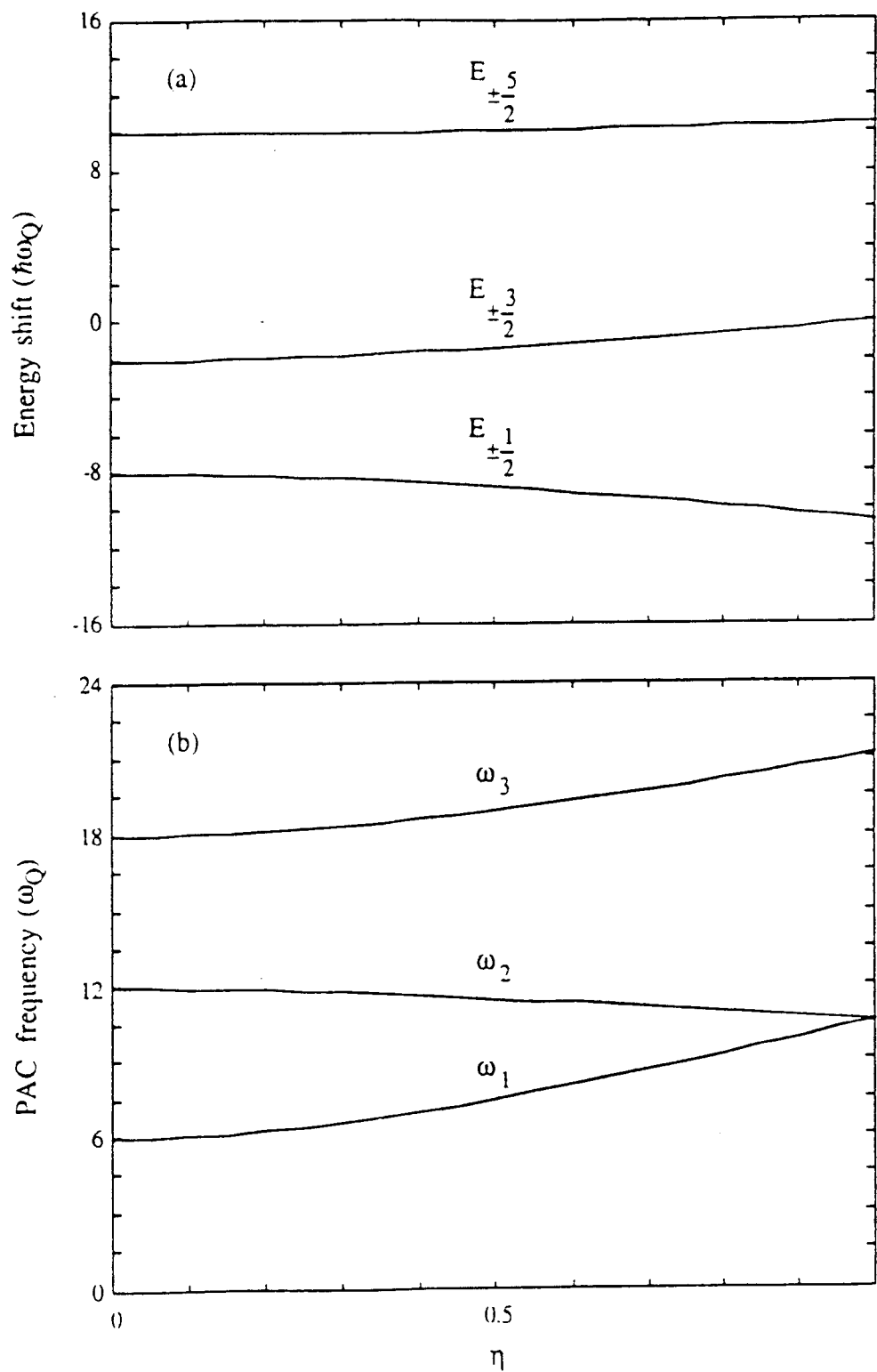


Fig. 3.3 a.) Eigenvalues and b.) PAC frequencies of the H_Q as function of η for $I = 5/2$.

From Eq.(3-26) we recall for a powder sample that the angular correlation is

$$W(\theta,t) = \sum_{\substack{k=0 \\ \text{even}}}^{k_{\max}} A_{kk} G_{kk} P_k(\cos\theta) ,$$

while Eq. (3-25) gave

$$G_{kk}(t) = \sum_n S_{nn}^{kk} + \sum_{n \neq n'} S_{nn'}^{kk} \cos \left(\frac{(E_{(n)} - E_{(n')}) t}{\hbar} \right),$$

Now for a nonaxisymmetric case this becomes

$$G_{kk}(t) = S_{n_0}(\eta) + \sum_{n=1}^3 S_{kn}(\eta) \cos(\omega_n(\eta) t). \quad (3-48)$$

We have tables or computer programs for the S_{kn} coefficients as a function of η .

3.5 The a-b fluctuation model

The main objective of these PAC experiments, as for all experiments, is to gain physical understanding of the measured spectra. In chapter 3 it was assumed that there are only static interactions, but this is not necessarily true, especially at higher temperatures. In order to describe this dynamic behavior, a more sophisticated model, which includes the effect of a fluctuating electric field gradient, is the a - b fluctuation model by William E. Evenson et al. [12]. Here it is assumed that lattice EFG can be observed within the lifetime of the intermediate state, $t_{1/2} = 84$ nsec.

Here it is assumed that with higher temperatures some oxygen atoms from the O1 - plane leave the unit cell, as is known from neutron diffraction measurements. The remaining O1 atoms fluctuate in the O1 plane on the a and b - axis. With an

increase in temperature the remaining oxygen atoms move faster in the O1 - plane so that one receives an average over the EFG as well as for the asymmetry η . Figure 3.4 explains the 2-dimensional fluctuation model for a PAC spectrum with the $R(t)$ on the left side and the Fourier transform on the right side. Fig. 3.4a.) shows the static spectra of a PAC measurement for $\text{YBa}_2\text{Cu}_3\text{O}_{7-x}$ with $\eta = 0.5$ while Fig. 3.4b.) - e.) has an increase in the fluctuation rate. In picture d.) to e.) it is assumed that a phase transition to a tetragonal structure occurred and so $\eta = 0$ as for $\text{YBa}_2\text{Cu}_3\text{O}_6$. Between the transition it is important to notice that a sufficient decrease of the amplitude and a line broadening occurs.

As is known from chapter 3.4, the perturbation factor $G_{22}(t)$ can be written for the static case as :

$$G_{kk}(t) = S_{no}(\eta) + \sum_{n=1}^3 S_{kn}(\eta) \cos(\omega_n(\eta) t), \quad (3-48)$$

where the dynamic case is given by:

$$G_{22}(t) = \sum_q G_q \exp[(-\lambda_q + i\omega_q)t] \quad (3-50)$$

G_q = complex coefficient, with q an index to the eigenvalues of the Blume matrix which includes all transition components of the spin $5/2$ state. There can be up to 15 distinct complex eigenvalues.

λ_q = damping factor

ω_Q = electric quadrupole splitting frequency

The influence of the fluctuation rate "w" on G_{22} is due mainly to the damping factor λ_q , shown approximately in Fig. 3.4.

Figure 3.4 The influence of G_Q by the fluctuation rate w

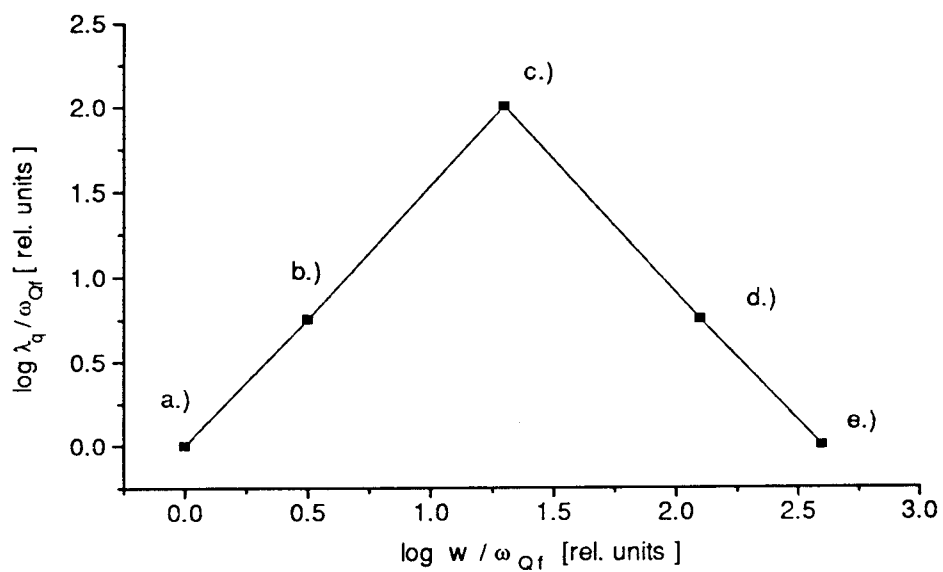
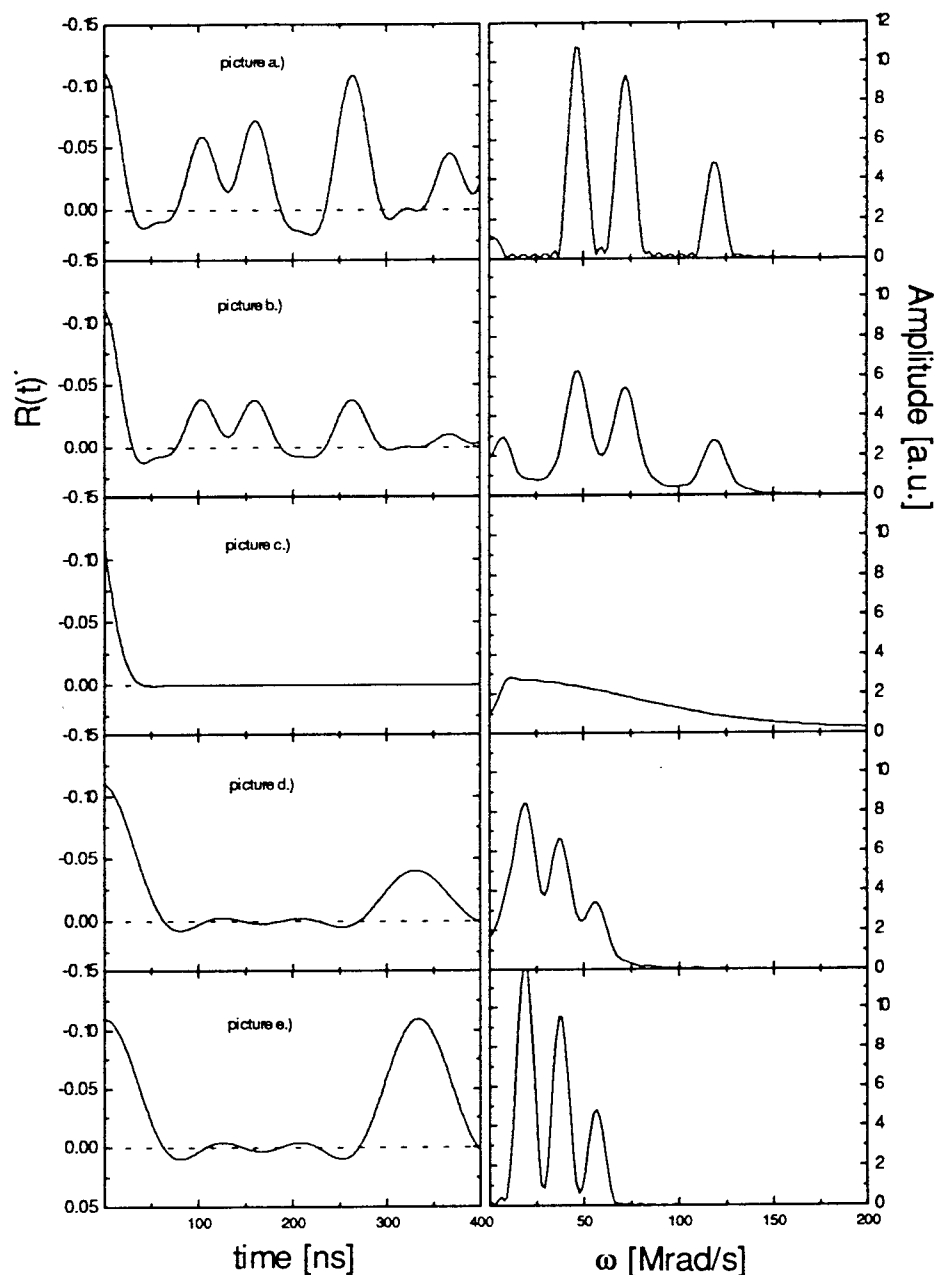


Figure 3.5 The theoretical Fourier transform for $\text{YBa}_2\text{Cu}_3\text{O}_{7-x}$ depending on the fluctuation rate



From Fig. 3.4 it is possible to see that there are two cases of interest, one where there is a slow fluctuation, low temperature, $\omega < \omega_{qf}$ and the other case is a rapid fluctuation, high temperature, compared to $t_{1/2} = 84$ nsec.

This can also be expressed by the following equations which can be derived from the general expression Eq.3.50

for case a.)

$$G_2(t) = \sum_{n=0}^3 \frac{\Lambda_n(\eta)}{\cos(\phi_n w)} e^{-\Delta_n w t} \cos(\omega_n(\eta) t - \phi_n w) \quad (3-51)$$

while for case d.)

$$G_2(t) = \sum_{n=0}^3 S_n(\eta) e^{-\Lambda_n t/w} \cos(\omega_n(\text{aver.}) t) \quad (3-52)$$

with :

w = fluctuation rate

ϕ_n = phase factor

$w \times \Lambda_n$ = damping factor

4. Experimental PAC setup

In the previous chapter it was shown that the angular correlation between two γ -rays, emitted from a nucleus, when subject to an extra-nuclear field, is not constant but will change with time. This behavior can be expressed with the perturbation factor from Eq.(2-25). The perturbation factor contains all the information about the interaction in the intermediate state, so that by measuring this factor we know everything about the interaction. In this section the experimental arrangements that are necessary to measure the perturbation factor will be explained.

Actually the change of the angular correlation over time is no more than the rotation of the decay characteristic with frequencies that are given by the interaction. For fixed detectors we get an oscillation of the coincidence rate over time, which is proportional to the rotation frequencies.

Our spectrometer for this time differential perturbed angular correlation (TDPAC) has the set-up shown in Fig. 4.1. At this time, it should be emphasized that the counting rate as a function of time is measured and not as a function of the angle. Hence exact time measurement is very important.

4.1 Coincidence electronics

From every detector we get two signals. The anode signal goes to the constant-fraction-discriminator where it is transformed to a sharp time signal. Afterwards the signal from detector 1 and 2 go to a mixer which gives the start signal while detector 3 and 4 yield the corresponding stop signal which is delayed by a cable for about 500 nsec. These two signals go then to a time-analog converter (TAC) which generates a pulse proportional to the start/stop time difference and are digitized by the analog-digital converter (ADC). For the time the ADC needs to digitize, the TAC is gated off by a busy signal.

The dynode signal supplies the energy pulses from each detector which are shaped and amplified by a preamplifier. A laboratory-built twin single-channel-analyzer (TSCA) is adjusted to detect the two energies, γ_1 and γ_2 , from the incoming bipolar pulses. The two energy signals from each TSCA are fed into a laboratory-built interface board. As soon as the TAC gets the time signals from the mixer it gives a true start to the interface board so that the corresponding energy signals

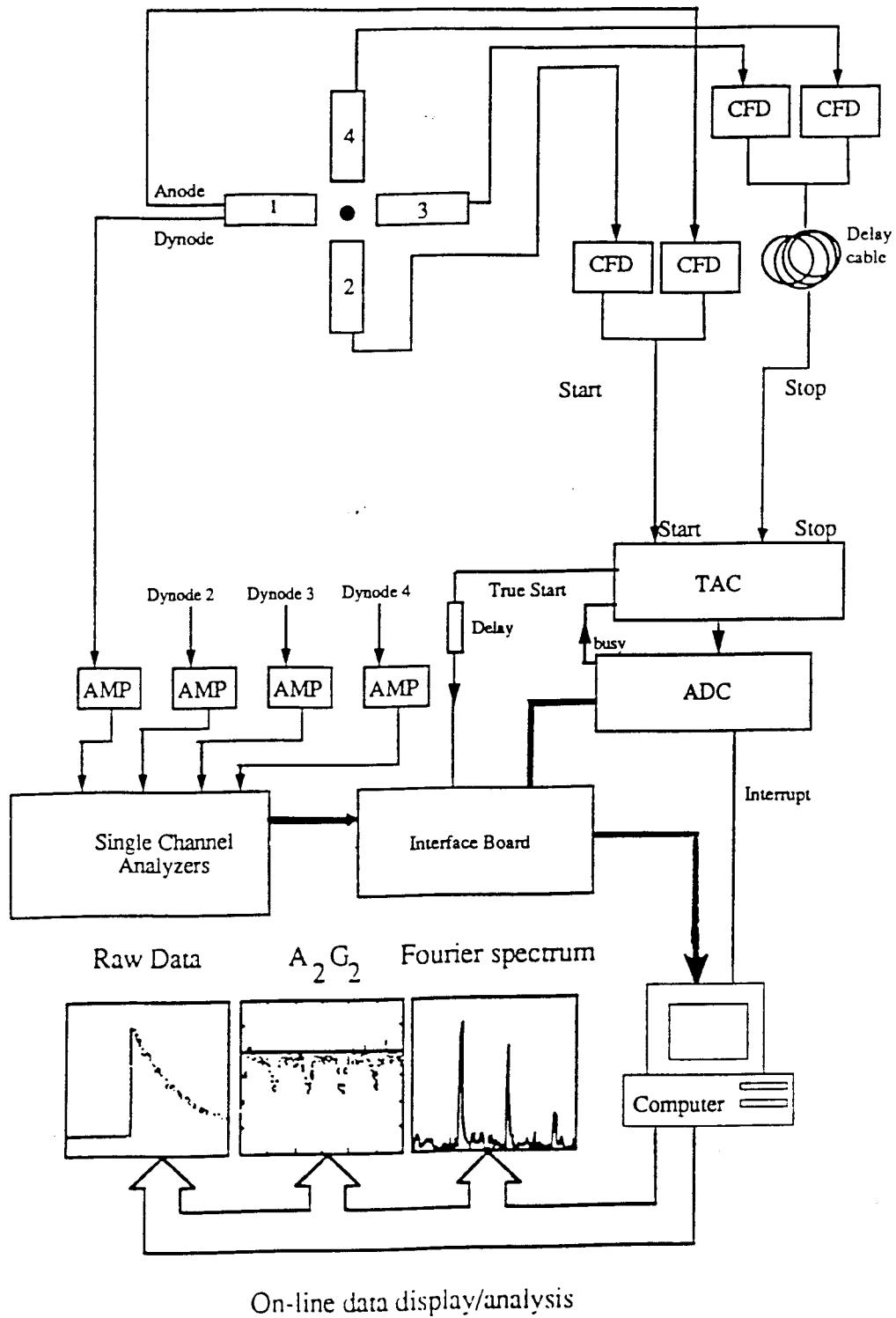


Fig. 4.1 Functional block diagram of the PAC spectrometer.

are transported to the digital I/O port of the computer. Here the energy signal is stored as soon as a valid event is flagged, the computer is interrupted when the ADC gives the computer the digitized time signal. From here the operating software calculates the raw data which can then be put on the screen.

A conversion is accepted as a valid "normal" event only if a TSCA of detector 1 or 2 indicates a γ_1 was detected and a TSCA of detector 3 and 4 indicates that a γ_2 was detected. If a γ_2 is detected by detector 1 or 2 and a γ_1 is detected by detector 3 or 4 then this is called a valid "reverse" event.

So the start - stop combinations are:

1 - 3	3 - 1
1 - 4	3 - 2
2 - 3	4 - 1
2 - 4	4 - 2
normal	reverse

4.2 Data analysis and evaluation

From a source with the activity N [13] every detector counts i γ -particles with the counting rate

$$N_i = \epsilon_i \Omega_i N$$

Where ϵ_i describes the sensitivity and Ω_i the solid angle. So we get a counting rate between start detector i and stop detector j of:

$$N_{ij} = N_i \epsilon_j \Omega_j = \epsilon_i \epsilon_j \Omega_i \Omega_j N$$

Beside the true coincidences we also have random events, these events depend on the time τ , within which γ_2 still counts as γ_1 , so we have to write:

$$N_{ij(\text{random})} = N_i N_j \tau = \epsilon_i \epsilon_j \Omega_i \Omega_j N^2 \tau$$

so we get a ratio of true events to random events of:

$$\frac{N_{ij}}{N_{ij(\text{random})}} = \frac{1}{N\tau}$$

In a TDPAC-experiment, τ is exactly the mean life time of the intermediate state τ_n , in case of ^{111}In $\tau_n = 85\text{ns}$. For example, if $t = 1\mu\text{s}$, the activity N of the sample

shouldn't be more than 10^6 decays per second in order to keep the ratio of true events to random events below 1.

The counting rate for a certain time window between the arrival of γ_1 and γ_2 is then given by:

$$N_{ij}(\theta,t) = N_0 e^{-t/t_n} W(\theta,t) + B$$

While B is the background counting rate, which is due to random events. $W(\theta,t)$ is the time dependent angular correlation function with θ the angle between two detectors. Usually 4 detectors are used which are structured in 90° see figure 4.1. With each detector combination and by subtracting the constant background counting rate B we get the following spectral ratio for the normal spectrum:

$$R_n(t) = \frac{2}{3} \left(\sqrt{\frac{N_{13}(180,t)N_{24}(180,t)}{N_{14}(90,t)N_{23}(90,t)}} \right)$$

and for the reverse spectra:

$$R_r(t) = \frac{2}{3} \left(\sqrt{\frac{N_{31}(180,t)N_{42}(180,t)}{N_{41}(90,t)N_{32}(90,t)}} \right)$$

For a static axially-symmetric electric field gradient we write Eq.(2-42) as:

$$W(q,t) = 1 + A_{22}G_{22}(t)P_2(\cos\theta) + \dots\dots\dots$$

here we neglected all terms with $k>2$. Under this assumption we get simply that with $|A_{22}| \ll 1$ the so defined spectral ratios are approximately:

$$R_{(t)} \approx A_{22}G_{22}(t)$$

where A_{22} is the effective anisotropy and $G_{22}(t)$ the experimental perturbation function.

The block diagram in figure 4.2 illustrates the data reduction process :

In the first figure we see one of the typical coincidence counting rates $N(\theta,t)$ which are used to fit the $A_{22}G_{22}(t)$ as we know from Eq.(3-2?a -b). Figure (b) shows us then one of these fitted $A_{22}G_{22}(t)$. In order to understand the data better a Fourier-analyses Fig. (c) is done which shows clearly the frequencies. Figure (d) and (e) gives us then the computer fit of $A_{22}G_{22}(t)$ and the Fourier transform.

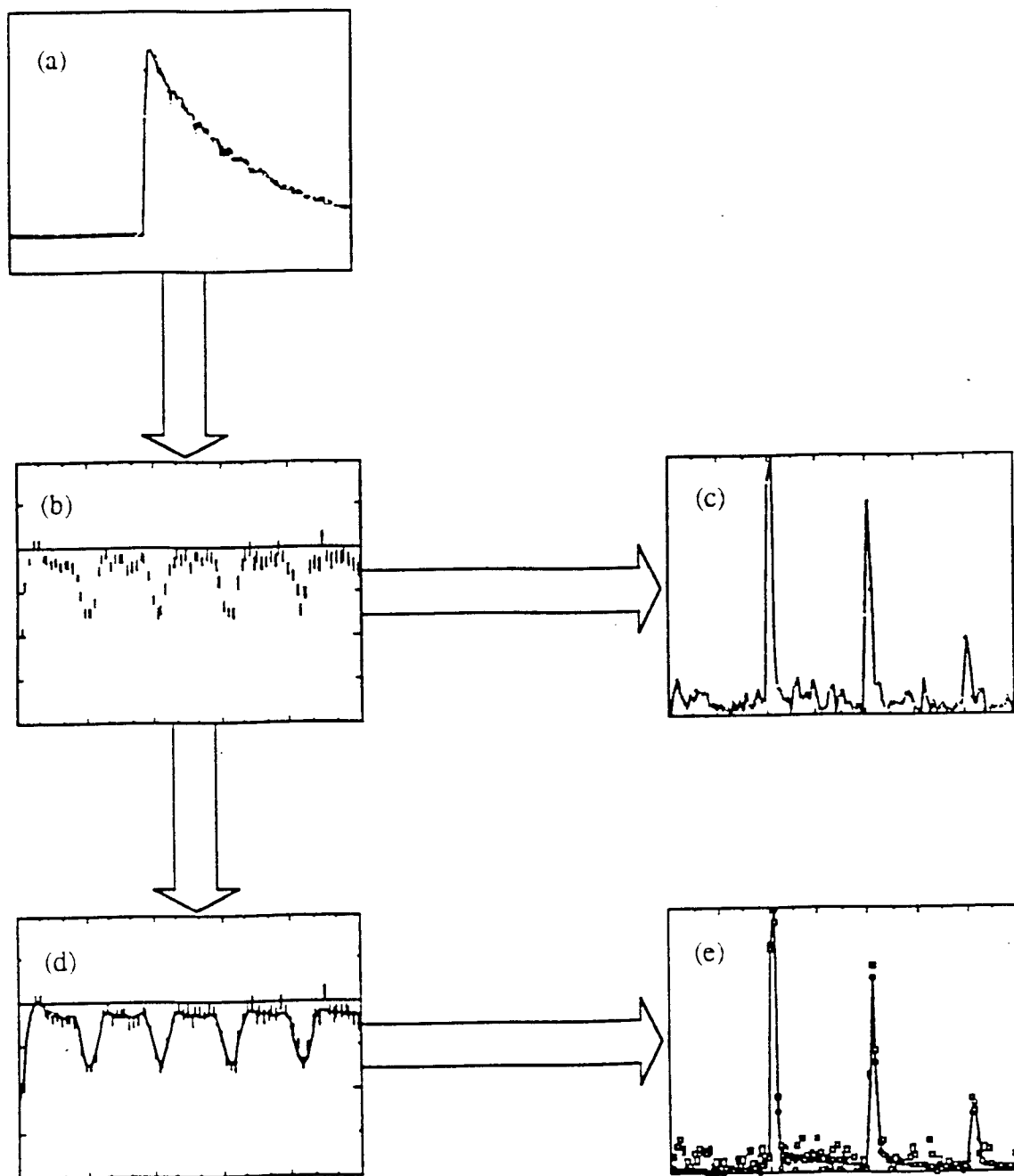


Fig. 4.2 The experimental $A_2G_2(t)$ b.) is computed from the background corrected coincident counts for a 90° and 180° detector pair, which is illustrated in a.). c.) the Fourier transform of b.) is performed to obtain a rough estimation of the PAC frequencies and number of possible sites. The computer fit to b.) is attempted and the time domain fit d.) and Fourier transforms for the fitted function and experimental $A_2G_2(t)$ are compared.

4.3 Fitted and derived PAC parameters

The counting ratio $R(t)$ is fitted with a least-squares fitting routine to the following theoretical function:

$$R(t) = A_{\text{eff}} \cdot \sum f_i \cdot \left(S_{\text{no}}(\eta)_i + \sum_{n=1}^3 S_{\text{kn}}(\eta)_i \cos(\omega_n(\eta) t)_i \right) \cdot \exp(-\Delta\omega_n t)_i$$

The f_i is the fraction of In probes that see the same surrounding (hyperfine field) and are normalized with $\sum f_i = 1$. The exponential factor accounts for the presence of small variations in the field and hence slight deviations in the probe site. For each site a Lorentzian broadening is assumed. Where $\Delta\omega_n$ is the difference of the frequencies $\omega_1, \omega_2, \omega_3$.

For $\omega_n(\eta) = 0$ we get an exponential fraction which we write as $f_{\text{exp}} \cdot e^{-\sigma_d t}$

In the case that $\sigma_d = 0$, we get the cubic fraction f_c .

Hence, the theoretical function can also be written as:

$$R(t) = A_{\text{eff}} \cdot \left(f_c + f_{\text{exp}} \cdot e^{-\sigma_d t} + \sum_i f_i \cdot \sum_{n=0}^3 S_{\text{kn}}(\eta) \cos(\omega_n(\eta) t) \cdot \exp(-\Delta\omega_n t) \right)$$

with $\sum f_i = 1, \quad \sum s_n = 1$

in the fitting routine the following fit parameters are introduced:

A_{eff}	is the effective anisotropy which was described above and for powder samples is typically fixed to -0,11 if ^{111}In is used
f_c	the cubic fraction
f_{exp}	the exponential fraction
σ_d	the relaxation rate
f_i	describes the corresponding fractions of the observed phases

$\omega_1, \omega_2, \omega_3$ are the PAC frequencies which depend on the strength of the interaction between the nuclear quadrupole moment and the EFG due to the environment and asymmetry of the EFG

$\sigma_1, \sigma_2, \sigma_3$ represent the relative distribution of the EFG, $\sigma = \frac{\Delta\omega}{\omega}$, is also called the line width

η describes the asymmetry of the EFG and lies between $0 \leq \eta \leq 1$
 v_a is the asymmetry parameter and is related to ω_i , see here to Eq.(3-31)

S_{kn} are the amplitudes, which depend on the orientation but are known functions of eta for random polycrystals.

so for polycrystalline samples we can write:

$$s_0 = 0.19$$

$$s_1 = 0.37$$

$$s_2 = 0.28$$

$$s_3 = 0.16$$

4.4 The effective anisotropy A_{eff} of ^{111}Cd

The actual theoretical value of the anisotropy in ^{111}Cd is $A_{\text{eff}} = -0.18$ where in the experiment A_{eff} has to be modified. This is due to the fact that:

- the samples never have the ideal form of a point \Rightarrow lowering of the effective anisotropy
- the function is averaged over the solid angle, and the solid angle depends on:
 - the detectors only have a finite size \Rightarrow lowering of the effective anisotropy
 - the distance between detector and sample influence A_{eff} \Rightarrow further away gives an increase of the effective anisotropy
- the activity of the sample can influence the A_{eff} \Rightarrow if the count rate is very high a decrease of the effective anisotropy can be observed which is due to random misrouting effects.

From the experiment typically a value of $A_{\text{eff}} = -0.11$ can be derived from $R_{(t=0)}$ and is thus well known, since:

$$R(t) \approx A_{\text{eff}} \cdot G_{22}(0)$$

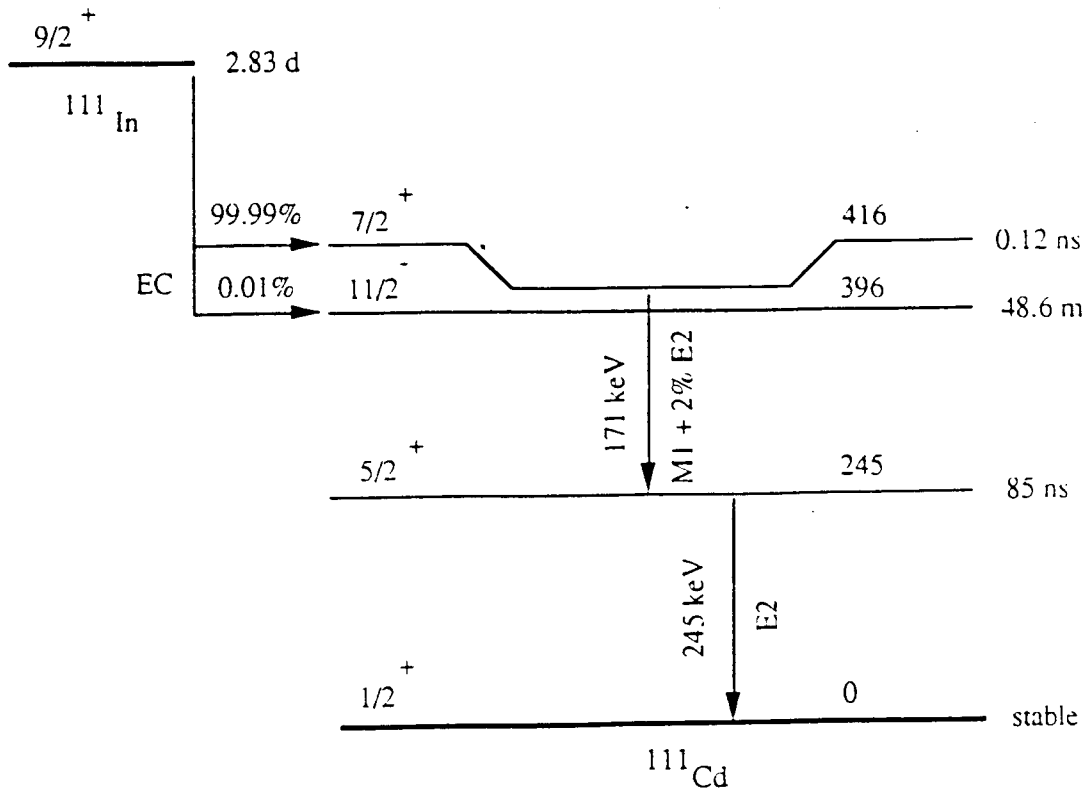
and

$$G_{22}(0) = 1.$$

4.5 Probe nuclei for PAC spectroscopy

An isotope is useful for PAC if it has certain properties which are considered below. One of the main requirements is the presence of an isomeric state with a life time between 10ns and a few μs . The short time limit is determined by the time resolution of the instrumentation, while the long measuring times are limited by the probability of accidental coincidences. The isomeric level should have a large quadrupole moment ($Q \geq 0.1$ barn) and if magnetic interactions are measured the magnetic dipole should be at least ($\mu \geq 1\mu_n$).

A γ - γ -cascade has to be present, with the isomer level as an intermediate state which should have a big anisotropy of the angular correlation.



parent half-life of ^{111}In	2.83 days
energies of cascade gamma-rays:	
gamma 1	171.28(8) keV
gamma 2	245.42(7) keV
Angular-correlation coefficients:	
A22	-0.18(2)
A44	+0.002(1)
A24	-0.204(2)
A42	-0.001(1)
Intermediate nuclear state:	
half-life	85.0(7) ns
elec. quadruple moment	+0.83(13) b
mag. dipole moment	-0.7656(25) μ_n

Fig. 4.3 The ^{111}In to ^{111}Cd decay in a schematic diagram [9].

In practice, the main sources used for PAC are ^{111}In , ^{181}Hf and ^{100}Pd . The corresponding daughter isotopes in which the PAC-measurements are done are ^{111}Cd , ^{181}Ta and ^{100}Rh . In the following only ^{111}In will be discussed because it is the isotope used in this work.

The isotope ^{111}In , which decays by electron capture to ^{111}Cd , can be produced by either the following nuclear reactions $^{110}\text{Cd}(d,n)^{111}\text{In}$ or $^{109}\text{Ag}(\alpha,2n)^{111}\text{In}$. The indium can be separated from the target substance by a chemical process so the activity is almost carrierfree.

The indium substance can then be bought as indium chloride dissolved in HCl liquid. After evaporating the solution, ^{111}In can either be introduced into the sample by diffusion or by ion implantation. It is important to mention that often only 10^{10} - 10^{12} atoms of ^{111}In are used in the sample. Hence the probe atom is very dilute in the sample, compared to 10^{18} probe atoms in NMR for example. Figure 4.3 shows the decay process of ^{111}In .

^{111}In is the most widely used PAC-source, its importance for PAC is similar to the importance of ^{57}Co for the Mößbauer effect.

4.6 Accuracy of the temperature measurements

The furnace used in this work, is built around a closed-one-end alumina furnace tube with an inner diameter of 3/8" and an outside diameter of 1/2". The heating element is cut from a 0.005" thick graphite foil and wrapped around the furnace tube. The pattern for the heating element was so chosen that no magnetic field could be created, so the measurement could not be influenced. Then the heating element is covered with one layer of organic binder-free alumina thermal insulation and two layers of zirconium foil. When the high-temperature furnace was designed, the following constraints applied to it:

- The outer surface of the furnace must be at room temperature independent of the sample temperature.
- The furnace must work reliably at a temperature of 1400°C continuously over several weeks.
- In order to accomplish such high temperatures the furnace has to be able to withstand a vacuum of 10^{-2} Torr.

The open end of the furnace is exposed to the air, and the sample and a Pt-Pt/10%Rh thermocouple is placed in the center of the tube. The temperature is controlled by a microprocessor-based digital controller (Eurotherm Corporation, Reston, Virginia, model 808) connected to the thermocouple as well as to the computer. So the temperature could be set by the computer to any temperature.

The accuracy of the thermocouple was obtained by calibrating the whole configuration in ice water, in order to set the 0°C point, and at 100°C by boiling water, the error was found to be 1°C.

The accuracy of the temperature controller was listed with 1°C by the manufacturer.

During the measurement the thermocouple was sitting beside the sample which was placed at the hottest point of the furnace. Around the sample the temperature differed only by 1°C two centimeter above and below the sample.

5. Overview of PAC measurements on $\text{YBa}_2\text{Cu}_3\text{O}_{7-x}$ and related compounds

5.1 PAC measurements on $\text{YBa}_2\text{Cu}_3\text{O}_{7-x}$ from the literature

There are several groups that have attempted PAC - measurements of $\text{YBa}_2\text{Cu}_3\text{O}_{7-x}$. The $5/2$ state at 245 keV in ^{111}Cd was the most frequently used PAC hyperfine probe. Different methods have been applied to introduce the nuclear tracer typical are:

- Implantation of ^{111}In in $\text{YBa}_2\text{Cu}_3\text{O}_{7-x}$ and single $\text{YBa}_2\text{Cu}_3\text{O}_{7-x}$ crystal where the probe stop at a mean depth of about 60nm. In order to reduce the effects of the radiation damage, the samples were annealed in air at a temperature of about 700°C and afterwards annealed in O_2 at 500°C to restore the orthorhombic phase [15].
- Diffusion of the In activity into $\text{YBa}_2\text{Cu}_3\text{O}_{7-x}$ at 1220K with an oxygen pressure of 10^5Pa for 15h, the samples were then slowly cooled down with a rate less then $1^\circ\text{C}/\text{min}$ [14].

Table 5.1 gives a summary of the experimental results obtained by some groups and their interpretation about the substitution of ^{111}In in $\text{YBa}_2\text{Cu}_3\text{O}_{7-x}$.

Most groups report difficulties in substituting ^{111}In into $\text{YBa}_2\text{Cu}_3\text{O}_{7-x}$ and obtaining reproducible results. Based on the measured PAC results , point - ion model calculation and chem. considerations all indicates that indium substitutes at either a Y- or Cu - site.

Table 5.1 The PAC parameters of ^{111}Cd in $\text{YBa}_2\text{Cu}_3\text{O}_{7-x}$ measured at RT by other groups and their interpretation.

site	ν_Q (MHz)	η	ω_1 mrad/sec	reference
Y-site	39(1)	0.3(1)	40(1)	14
Cu1-site in tetra. phase	134(1)	0	126(1)	15
Cu1-site in ortho. phase	143(1)	1	237(1)	15
Ba-site	139(1)	0.4(1)	152(1)	14
Cu1-site in ortho. phase	156(1)	1	259(1)	16

As one can see a variety of possible sites for the probe atom in the lattice were assumed at the beginning of PAC measurements, where in our measurements only one site can be detected.

So R. Schwenker [9] interpreted his data that below the melting point of $\text{YBa}_2\text{Cu}_3\text{O}_{7-x}$ ^{111}In would be substitutional to the Yttrium site, whereas above the melting point a new fraction at $\nu_Q = 150$ MHz could be observed. This fraction was explained as ^{111}In being substituted at a copper site whose population increases rapidly with temperature. This fraction at $\nu_Q = 150$ MHz was not observed in these PAC measurements.

5.2 PAC measurements on $\text{YBa}_2\text{Cu}_3\text{O}_{7-x}$ related compounds from the literature

Although it seems to be possible from x-ray measurements to prepare pure polycrystalline samples there is always a small percentage of second phases like $\text{Y}_2\text{Ba}_1\text{Cu}_1\text{O}_5$ and starting material encountered in the end-product $\text{YBa}_2\text{Cu}_3\text{O}_{7-x}$. The sensitivity of x-ray measurements is determined by statistical uncertainties and usual values for detectible phases are $> 5\%$.

It is known that the nuclear tracer ^{111}In prefers the 211 phase and so a higher fraction of $\text{Y}_2\text{Ba}_1\text{Cu}_1\text{O}_5$ can be found by PAC despite the fact that the total quantity of 211 is actually lower than 5% in the sample. This is already motivation, table 5.2, enough to study the PAC parameters of ^{111}In in related compounds of $\text{YBa}_2\text{Cu}_3\text{O}_{7-x}$ to make sure that there is no misinterpretation of the data. High temperature measurements above the decomposition temperature of 1-2-3 can also provide information on identification of which phases are associated with particular sites found in PAC spectra.

Table 5.2 A summary of the PAC investigations done by several groups on compounds that could be formed as minority phases.

material	f[%]	ω_1 [10^{-6}]	ω_2 rad/sec]	η	δ	T [°C]	reference
Y ₂ O ₃	51	138	276	0	10	RT	16
	11	95	124	0.7	4		
	38	50	100	0	48		
	77.3	133	167	0.73	0.93	1200	17
	22.7	148	292	0.02	0.2		
InO ₃	75	160	208	0.69	4	RT	18
	25	145	290	0	4		
	72.3	160	208	0.69	0.48	1000	19
	27.7	147	291	0.04	0.57		
Cu ₂ O	78	257	399	0.49	15	RT	20
	22	145	173	0.79	4		
	81	235	425	0.29	2	400	20
	19	139	167	0.78	4		
	85	243	418	0.36	30	500	20
	15	160	162	0.98	22		
	95	212	366	0.36	53	900	20
	5	114	146	0.7	4		
CuO	81	222	339	0.51	19	RT	20
	19	117	169	0.57	5		
	81	217	312	0.58	15	500	20
	19	119	151	0.72	3		

5.3 Calculation of the electric field gradient (EFG) for $\text{YBa}_2\text{Cu}_3\text{O}_{7-x}$ and related components

Since the electric field gradient is the second derivative of the external electric potential it can be derived the following way.

The EFG can be derived in the following way for a single point charge.

$$\text{Electric Potential: } \phi(r) = \frac{1}{4\pi\epsilon_0} \times \frac{zq}{r} \quad \text{with } r = \sqrt{x^2+y^2+z^2} \quad (5-1)$$

Since the electric field is the first derivative we get

$$E(r) = \frac{-\partial\phi(r)}{\partial x_i} = \frac{zq}{4\pi\epsilon_0} * \frac{\partial}{\partial x_i} \frac{1}{r} = \frac{zq}{4\pi\epsilon_0} \begin{pmatrix} \frac{x}{r^3} \\ \frac{y}{r^3} \\ \frac{z}{r^3} \end{pmatrix}. \quad (5-2)$$

The electric field gradient is finally defined as

$$V^{(0)}_j = \frac{\partial E(r)}{\partial x_j} = \frac{-zq}{4\pi\epsilon_0} * \frac{1}{r^5} \begin{pmatrix} 3x^2-r^2 & 3xy & 3xz \\ 3xy & 3y^2-r^2 & 3yz \\ 3xz & 3yz & 3z^2-r^2 \end{pmatrix}, \quad (5-3)$$

so the electric field gradient can be written for a system of point charges, each of charge Zq , at position r_i with respect to zero.

$$V^{(0)}_{\alpha\beta} = \frac{1}{4\pi\epsilon_0} * \sum_{i \neq 0} \frac{-z_i q_i}{r_i^5} \begin{pmatrix} 3x_i^2-r_i^2 & 3x_i y_i & 3x_i z_i \\ 3x_i y_i & 3y_i^2-r_i^2 & 3y_i z_i \\ 3x_i z_i & 3y_i z_i & 3z_i^2-r_i^2 \end{pmatrix} \quad (5-4)$$

It is also often usual to define an asymmetry parameter called " η " which is simply the ratio of:

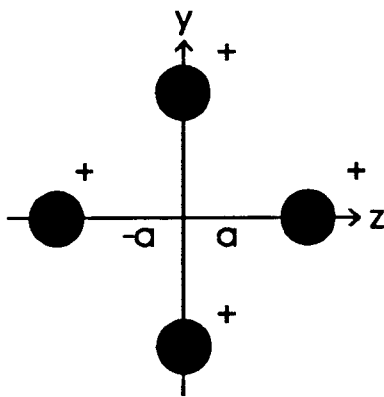
$$\eta = \frac{V_{yy} - V_{xx}}{V_{zz}} \quad (5-5)$$

where the definition for the components of the electric field gradient is given as:

$$|V_{zz}| > |V_{yy}| > |V_{xx}|$$

which means that the components are relative to the chosen main coordinate system.

In the following some simple examples for the calculation of the electric field gradient shall be given in order to achieve a better understanding of this tensor quantity.



so: $r = a$

case a:) all charges are positive

$$\Rightarrow V_{\alpha\beta} = \frac{-zq}{4\pi\epsilon_0} * \frac{1}{a^5} \left(\begin{pmatrix} -a^2 & 0 & 0 \\ 0 & -a^2 & 0 \\ 0 & 0 & 2a^2 \end{pmatrix} + \begin{pmatrix} -a^2 & 0 & 0 \\ 0 & -a^2 & 0 \\ 0 & 0 & 2a^2 \end{pmatrix} + \begin{pmatrix} -a^2 & 0 & 0 \\ 0 & 2a^2 & 0 \\ 0 & 0 & -a^2 \end{pmatrix} + \begin{pmatrix} -a^2 & 0 & 0 \\ 0 & 2a^2 & 0 \\ 0 & 0 & -a^2 \end{pmatrix} \right)$$

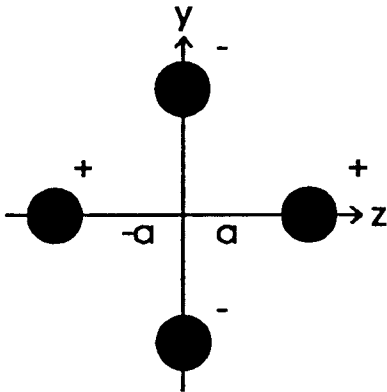
$$V(0) = \frac{-zq}{4\pi\epsilon_0} * \frac{1}{a^5} \begin{pmatrix} -4a^2 & 0 & 0 \\ 0 & 2a^2 & 0 \\ 0 & 0 & 2a^2 \end{pmatrix}$$

so we know that:

$$\left. \begin{array}{l} V_{zz} = -4a^2 \\ V_{yy} = 2a^2 \\ V_{xx} = 2a^2 \end{array} \right\} * \frac{-zq}{4\pi\epsilon_0} * \frac{1}{a^5} \quad \eta = \frac{V_{yy} - V_{xx}}{V_{zz}} = 0$$

From $V(0)$ one can see that the V_{zz} component is perpendicular to the z-y plane. In this specific case the asymmetry is 0.

case b.) mixed charges



$$V_{\alpha\beta} = \frac{-zq}{4\pi\epsilon_0} * \frac{1}{a^5} \left(\begin{pmatrix} 2a^2 & 0 & 0 \\ 0 & 2a^2 & 0 \\ 0 & 0 & -4a^2 \end{pmatrix} + \begin{pmatrix} -2a^2 & 0 & 0 \\ 0 & 4a^2 & 0 \\ 0 & 0 & -2a^2 \end{pmatrix} \right) = \frac{-zq}{4\pi\epsilon_0} * \frac{1}{a^5} \begin{pmatrix} 0 & 0 & 0 \\ 0 & 6a^2 & 0 \\ 0 & 0 & -6a^2 \end{pmatrix}$$

$$\left. \begin{array}{l} V_{zz} = 6a^2 \\ V_{yy} = -6a^2 \\ V_{xx} = 0 \end{array} \right\} * \frac{-zq}{4\pi\epsilon_0} * \frac{1}{a^5} \quad \text{hence} \quad \eta = 1$$

This time the electric field gradient is in the plane and an asymmetry of $\eta = 1$ is observed. The only difference between case a.) and b.) is that mixed charges were assumed.

There are different models to calculate the electric field gradient for a crystal structure. The easiest one is the point-ion-charge model which is explained here. This model yields good results if the crystal behaves like an ion which means that nucleus, core electrons and the conduction electrons must be localized. But for calculations on a metal this model will be too simple since here the conduction electrons are not localized but free. Nevertheless this model is appropriate to show the tendency of the asymmetry parameter " η ", hence it was used in order to calculate the electric field gradient and the asymmetry parameter " η " for $\text{YBa}_2\text{Cu}_3\text{O}_7$ and $\text{Y}_2\text{Cu}_2\text{O}_5$ at various probe sites.

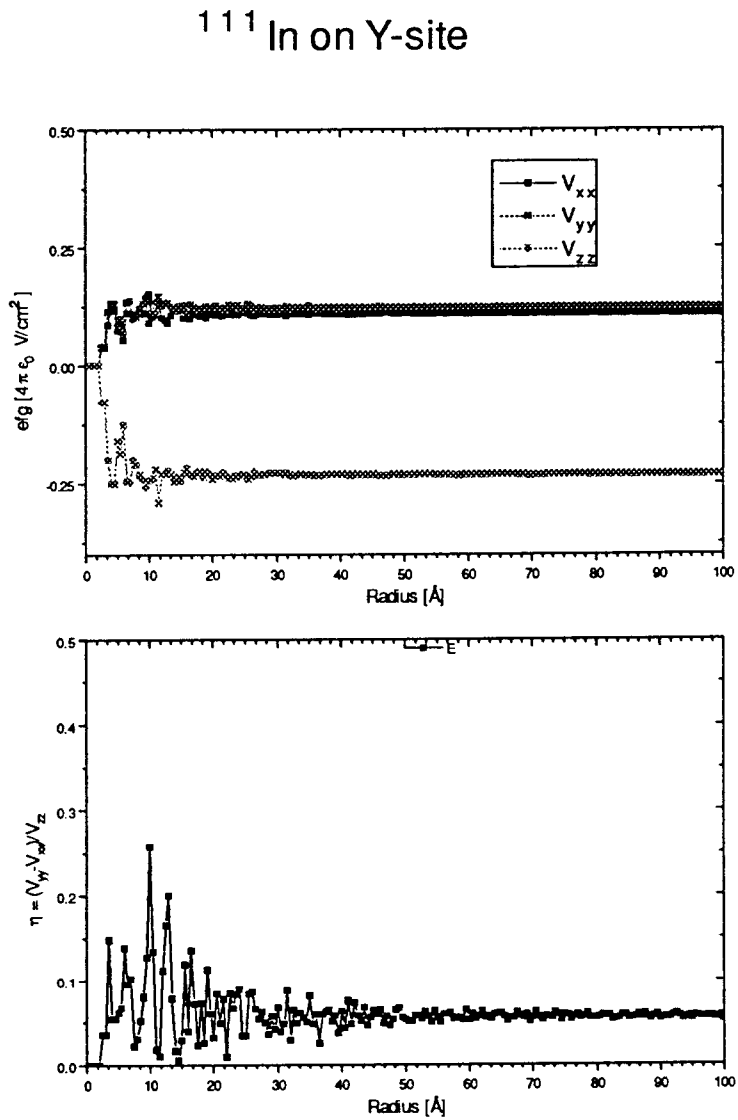
The following electric charges and radii were assumed for the atoms [27].

atom	charge	radius [10^{-10}m]	
Y	+3	0.93	
Ba	+2	1.35	
O	-2	1.40	
Cu	+2	0.69	for the Cu1-plane in $\text{YBa}_2\text{Cu}_3\text{O}_7$ and in $\text{Y}_2\text{Cu}_2\text{O}_5$
Cu	+3	0.69	for the Cu2-plane in $\text{YBa}_2\text{Cu}_3\text{O}_7$

Calculations of the electric charges for the atoms in $\text{YBa}_2\text{Cu}_3\text{O}_{7-x}$ were done by I.D. Brown et al.[22], here it was found that the values of the electric charges for Cu1 and Cu2 for $\text{YBa}_2\text{Cu}_3\text{O}_7$ is close to 2.33. By using these values only negligible changes for the asymmetry as well as for the EFG could be calculated compared to the values used above.

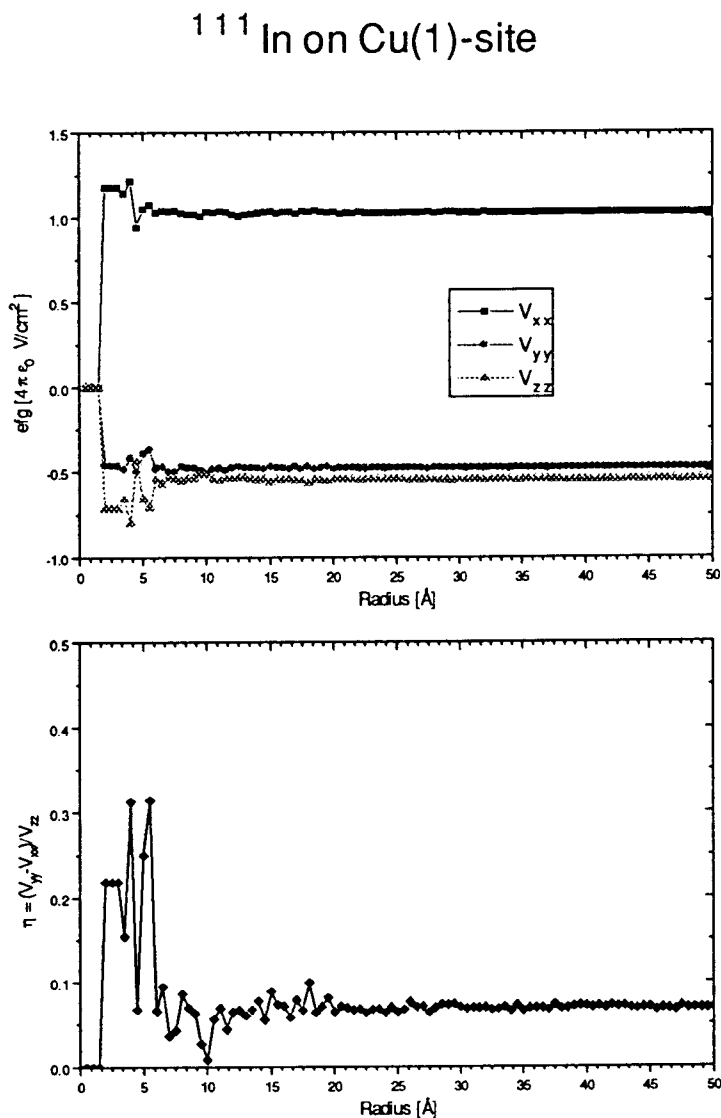
With these assumptions the following field gradient and asymmetry " η " could be calculated for ^{111}Cd in $\text{YBa}_2\text{Cu}_3\text{O}_{7-x}$ on an Y-site as seen in figure 5.1a.)-b). Figure 5.1a.) shows the behavior of the three components of the EFG vs. to the radius contributing more atoms around the Y - atom. Figure 5.1b.) contains the results for the respective asymmetry " η ". From both figures one can see the point where the parameters converge.

Fig. 5.1 a.) The calculated electric field gradient and b.) the asymmetry parameter η for $\text{YBa}_2\text{Cu}_3\text{O}_{7-x}$ on a Y-site



Next, calculations were done in the same way as before but for the Cu1 - site on $\text{YBa}_2\text{Cu}_3\text{O}_{7-x}$. Figure 5.2a.)-b.) shows us the result for this:

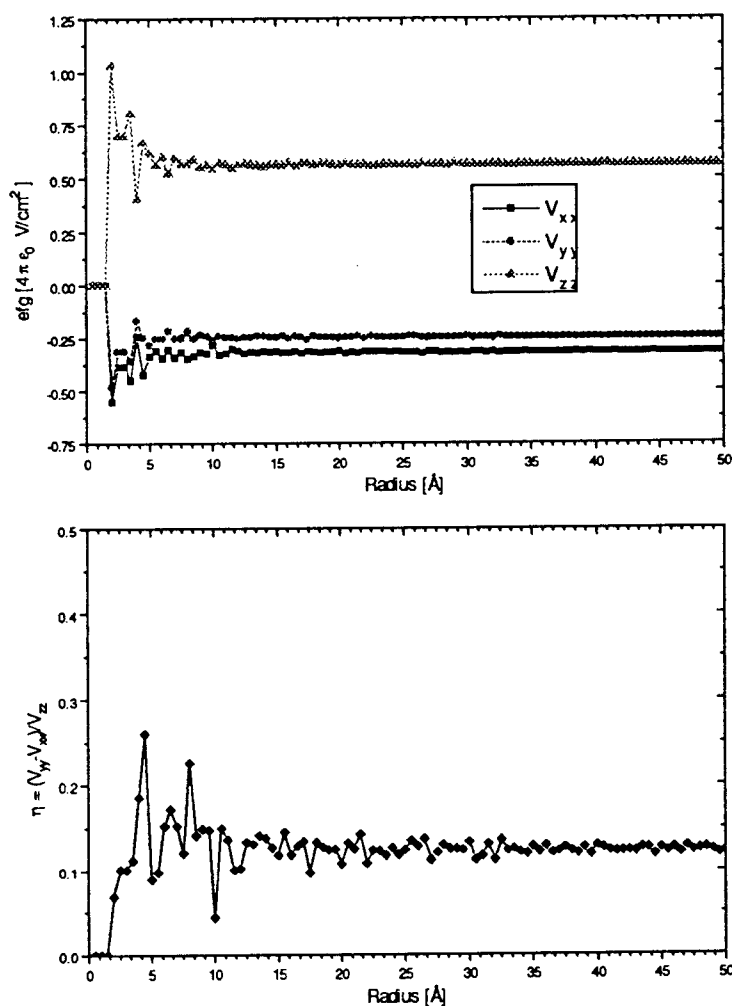
Fig. 5.2 a.) The calculated electric field gradient and b.) the asymmetry parameter η for $\text{YBa}_2\text{Cu}_3\text{O}_{7-x}$ on a Cu(1)-site



Finally the calculations were made on the Cu2 - site of $\text{YBa}_2\text{Cu}_3\text{O}_{7-x}$ here figure 5.3a.)-b.) refer to this calculation.

Fig. 5.3 a.) The calculated electric field gradient and b.) the asymmetry parameter η for $\text{YBa}_2\text{Cu}_3\text{O}_{7-x}$ on a Cu(2)-site

^{111}In on Cu(2)-site



The result from these calculations is that:

- The components of the EFG on the Cu1 site are higher than for Cu2 or Y
- The asymmetry η is small for both cases Cu1 and Y and slightly higher for Cu2
- Since the EFG has $1/r^3$ attenuation, there is only a slow convergence for all cases.

Beside the calculations for $\text{YBa}_2\text{Cu}_3\text{O}_{7-x}$ there were also calculations done on $\text{Y}_2\text{Cu}_2\text{O}_5$ again with respect to the probe site. Figure 5.4 to 5.5 a.)-b.) shows the result for calculations on the Y site in the first case and in the second case for the Cu1 site.

Fig. 5.4 a.) The calculated electric field gradient and b.) the asymmetry parameter η for $\text{Y}_2\text{Cu}_2\text{O}_5$ on a Y-site

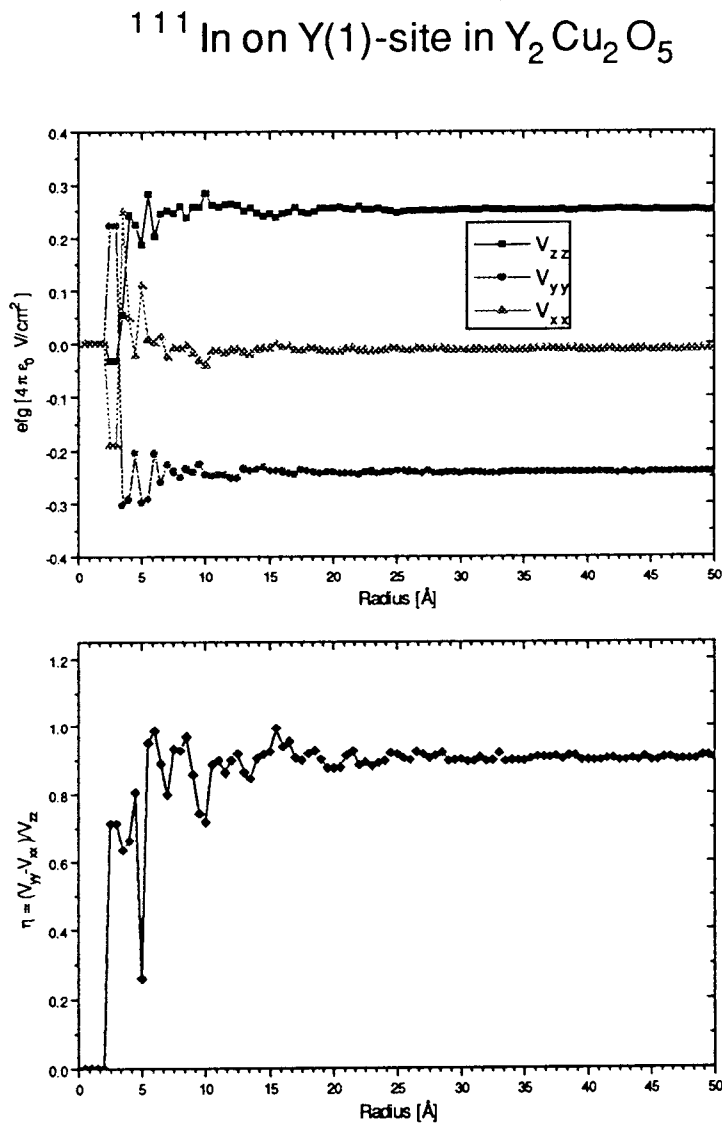
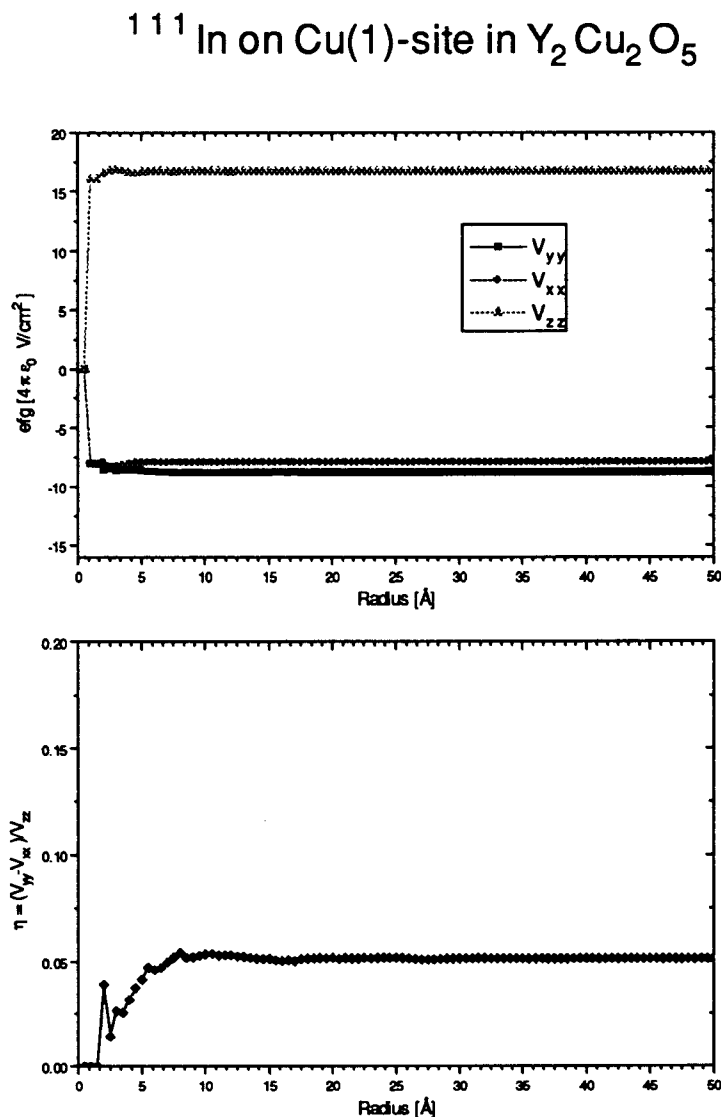


Fig. 5.5 a.) The calculated electric field gradient and b.) the asymmetry parameter η for $Y_2Cu_2O_5$ on a Cu-site



This time one can observe that the calculations on the Y site show big values for the asymmetry, with an η of almost 1, while the EFG components are relatively small compared to the values for the Cu1 site. Here one can observe large values for the EFG, about ten times bigger, but small values for the η . It is also interesting to notice that the convergence for the Cu1 site is much faster than for the Y site.

Other calculations for the electric field gradient on $\text{YBa}_2\text{Cu}_3\text{O}_{7-x}$ done by Ambrosch-Draxl and co. workers [28] get the following results and compare it with NQR and NMR measurements:

Position		V_{xx}	V_{yy}	V_{zz}	η
Y	Th.	-0.2	-3.2	3.4	0.9
Cu1	Th.	-6.7	7.4	-0.7	0.8
Cu1	Ex.	-7.4	7.5	0.0	1.0

5.4 The lattice position of ^{111}In in $\text{YBa}_2\text{Cu}_3\text{O}_{7-x}$

$\text{YBa}_2\text{Cu}_3\text{O}_{7-x}$ is a complicated component so that the question arises where does ^{111}In substitute in YBaCuO ?

It was already shown in section 5.1 that different groups attributed different PAC spectra to different lattice sites in $\text{YBa}_2\text{Cu}_3\text{O}_{7-x}$.

We see only one well-defined EFG, which means that our probe atoms experience the same unique surrounding. There is no possibility for our PAC method to determine the exact lattice location of ^{111}In .

However we believe that our probe atoms are substituting the Y-atoms. The reason for that are the chemical similarity of these two atom species. Both have the same number of valence electrons and nearly identical ionic radii.

$$r_{\text{Y}^{3+}} = 0.89 \text{ \AA} \quad ; \quad r_{\text{In}^{3+}} = 0.91 \text{ \AA}$$

While Cu^{2+} , Ba^{2+} have a totally different electronic configuration and radius.

$$r_{\text{Cu}^{2+}} = 0.69 \text{ \AA} \quad ; \quad r_{\text{Ba}^{2+}} = 1.35 \text{ \AA}$$

6. Experimental Results of the PAC measurements on $\text{YBa}_2\text{Cu}_3\text{O}_{7-x}$ and $\text{Y}_2\text{Cu}_2\text{O}_5$.

This chapter presents the PAC results found for 1-2-3 in flowing oxygen as well as in flowing air. The experimentally observed data were never fully reproducible, which is due to the fact that there are small changes in the sample preparation for each sample. After the decomposition of 1-2-3 new compounds were created, whose PAC patterns had been observed before and are reported in the literature. However sometimes they were claimed to be 1-2-3. To clarify this picture further PAC-experiments on the compounds 2-0-2 and 2-1-1 were carried out. All A_2G_2 spectra were fitted with the standard model for static interaction between the electric field gradient and quadrupole moment, static means the EFG is time independent, as described in chapter 3.

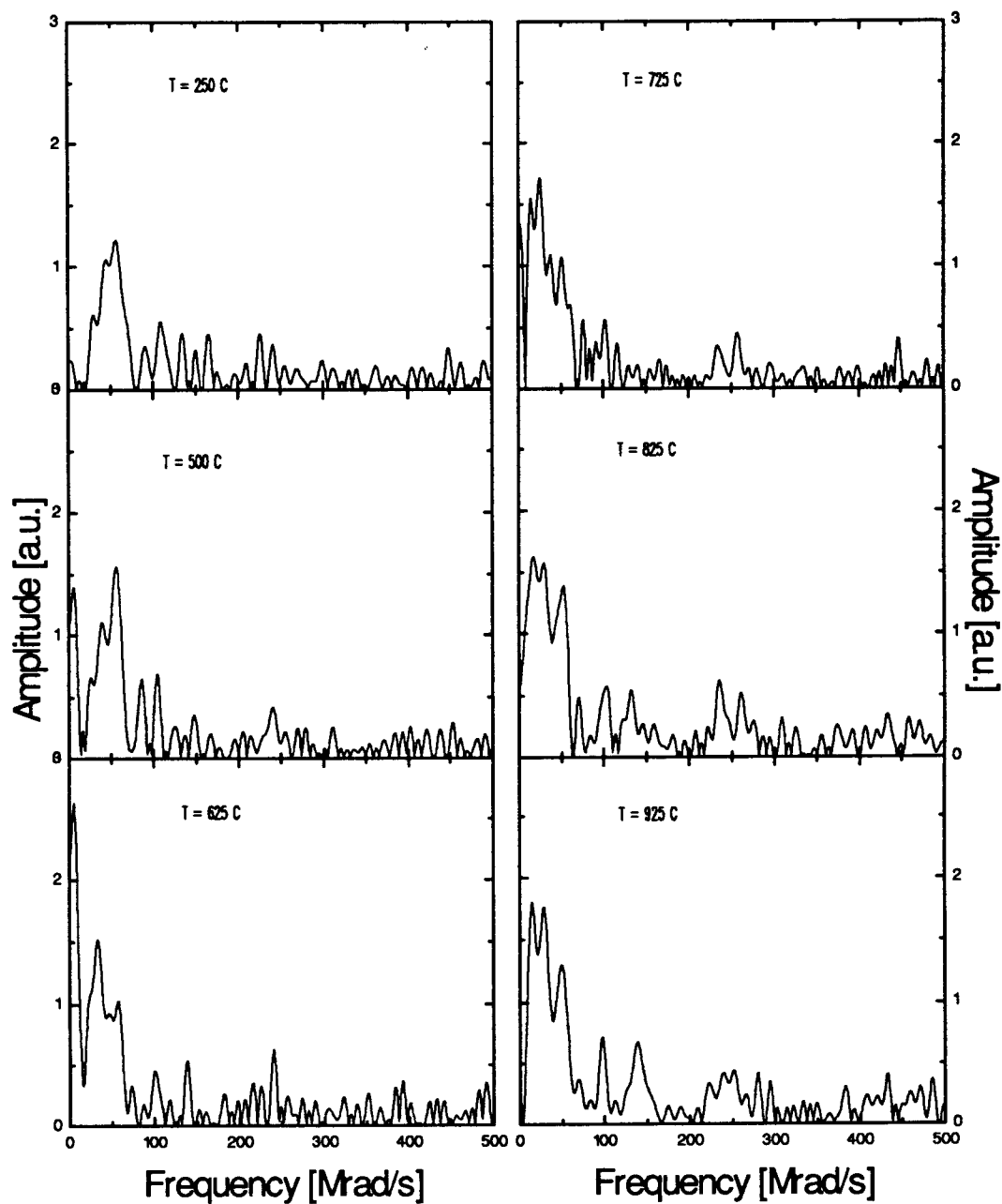
6.1 PAC data on $\text{YBa}_2\text{Cu}_3\text{O}_{7-x}$ in flowing oxygen

Neutron diffraction data shown in chapter 1. suggest that the oxygen partial pressure around the sample has an important influence on the lattice parameter of the superconductor when increasing the temperature Fig.1.3. For this reason measurements were taken where the sample was under well defined oxygen atmosphere. A constant flow had to be guaranteed since carbon reacts to CO_2 and attacks the sample. Figure 6.1 shows the Fourier transforms of a typical run.

The following sites could be observed during the measurement:

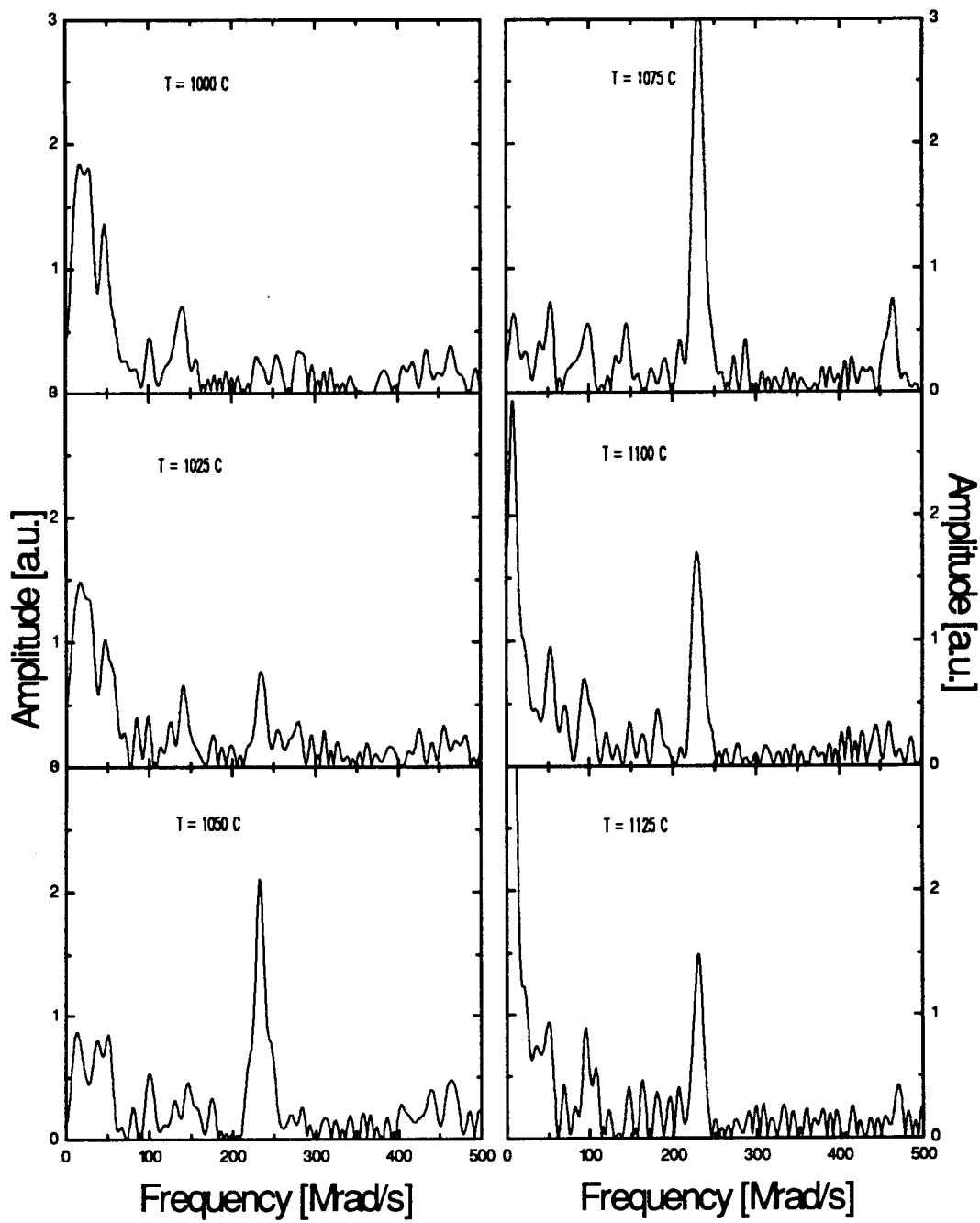
- site A at $\nu_Q = 36.4$ MHz for room temperature
- site B at $\nu_Q = 54$ MHz for room temperature
- site C at $\nu_Q = 142$ MHz for 1000°C
- site D at $\nu_Q = 0$ MHz above 1075°C

With an increase in temperature the frequencies of site A shift to lower values and at the same time the asymmetry " η " increases while the frequencies and asymmetry for site B stay constant. This behavior is constant up to temperatures of 1000°C. From then on the fraction of site A decreases and finally vanishes at 1050°C, which is also the decomposition temperature of $\text{YBa}_2\text{Cu}_3\text{O}_{7-x}$. At the same time where a decrease of site A can be observed a new site C at $\nu_Q = 240$ MHz appears. Above 1075°C site C as well as site B seem to start disappearing and instead a huge fraction at $\nu_Q = 0$ which shall be called site D appears. One can also observe that the suggested change, as shown in Fig.6.1, for the Fourier transform due to the a-b fluctuation does not occur.



in flowing oxygen

Fig.6.1 The Fourier transform of the time spectra obtained by PAC on $\text{YBa}_2\text{Cu}_3\text{O}_{7-x}$ for various temperatures in flowing oxygen



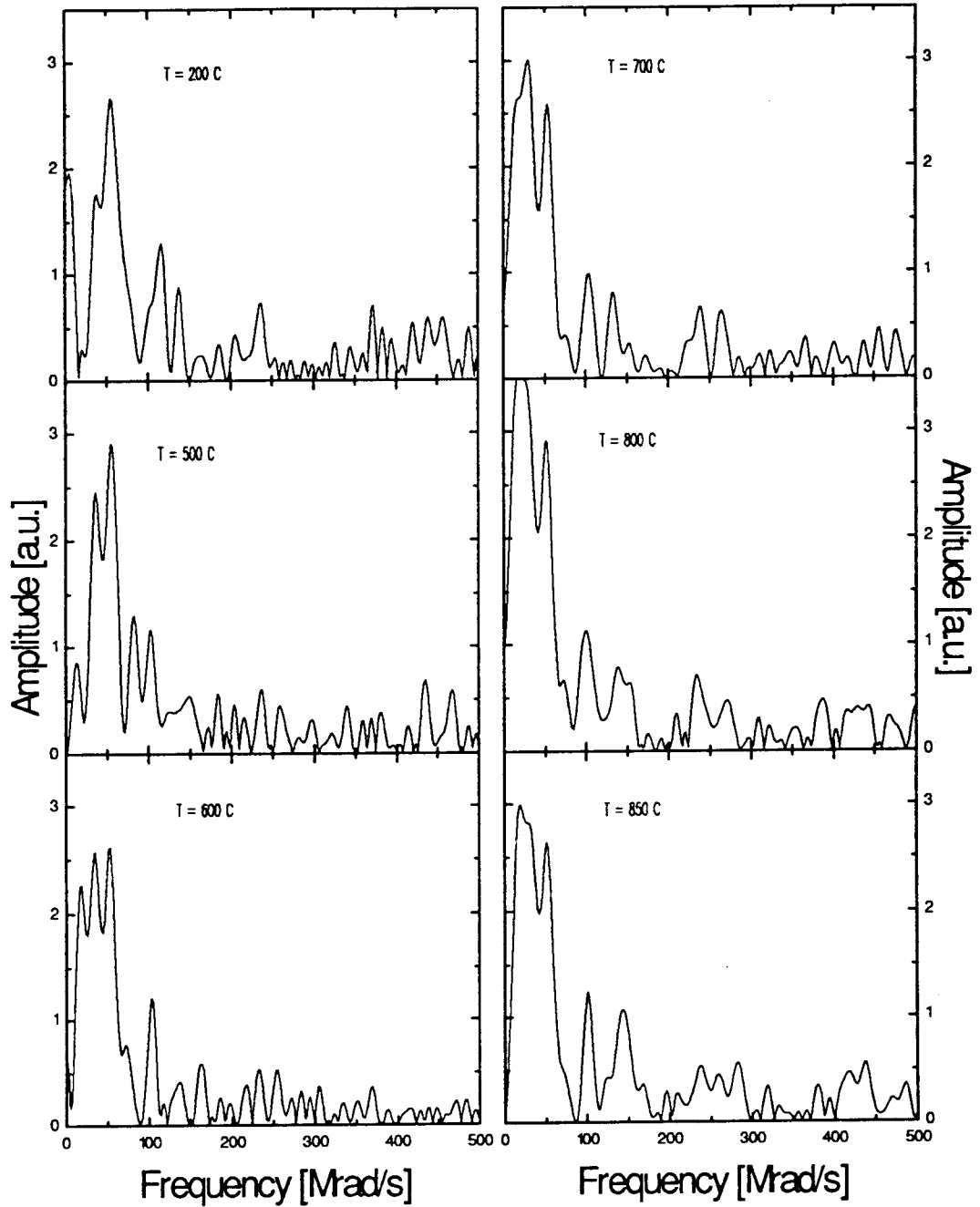
in flowing oxygen

cont. from Figure 6.1

6.2 PAC data on $\text{YBa}_2\text{Cu}_3\text{O}_{7-x}$ in flowing air

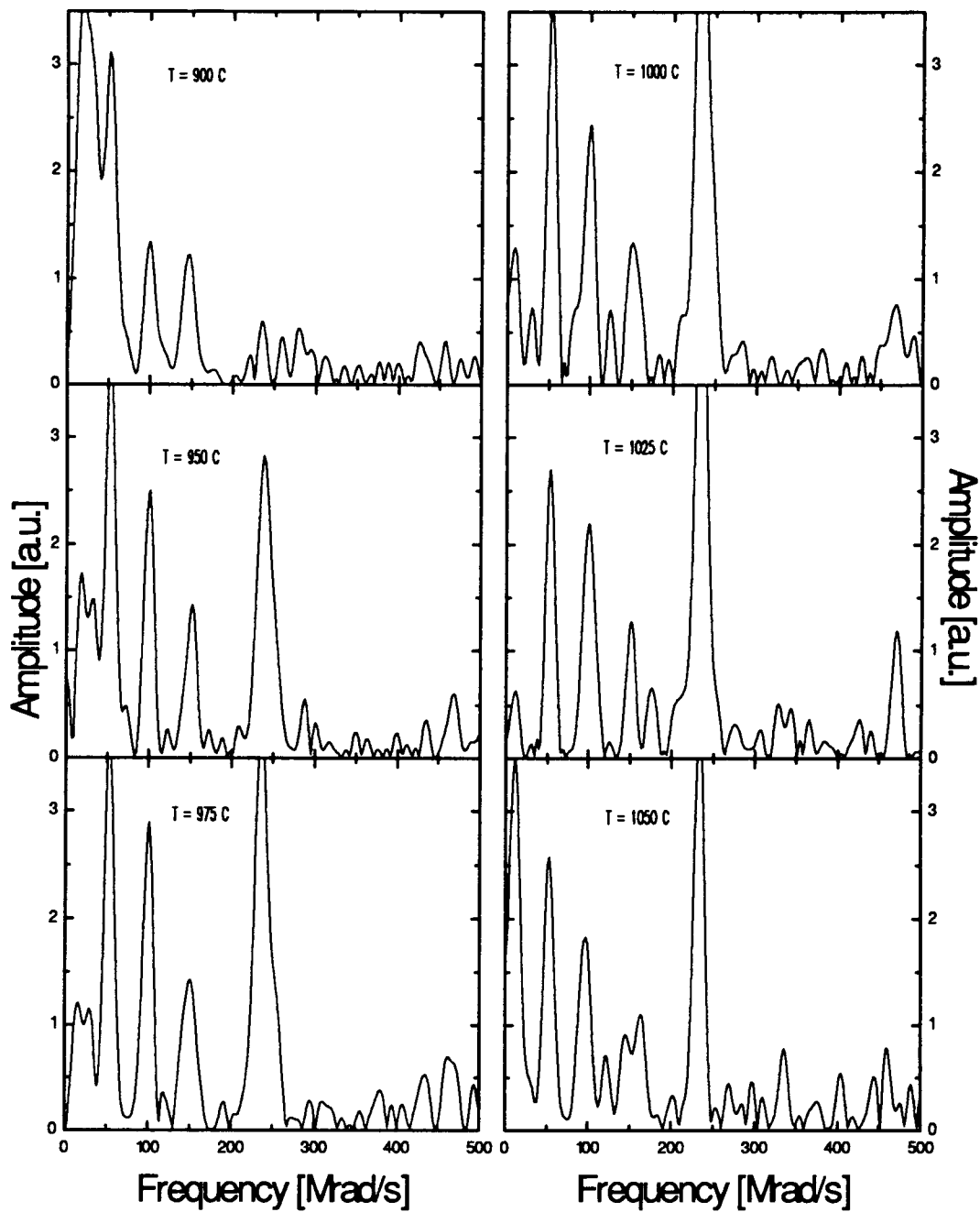
In order to compare the influence of oxygen on the superconductor measurements were taken while the sample was under a steady flow of air. Figure 6.2 shows a typical run.

At 200°C the same sites A and B are clearly present. With the rise in temperature the site A experiences an increase in η and the frequencies shift to lower values. This is the same behavior as was observed in flowing oxygen. Again, site B stays almost the same. The decomposition of site A occurs in this case between 900°C and 950°C while in flowing oxygen the disintegration of site A happened between 1000°C and 1050°C. This is the only difference since with a further increase of temperature the same behavior as before can be observed. The reason for this difference is obviously due to the different oxygen atmosphere that was used in both experiments and hence also had to influence the oxygen content of the material. Also here it can be seen that the suggested behavior for the a-b fluctuation can not be observed.



in flowing air

Fig. 6.2 The Fourier transform of the time spectra obtained by PAC on $\text{YBa}_2\text{Cu}_3\text{O}_{7-x}$ for various temperatures in flowing air.



in flowing air

cont. from Figure 6.2

6.3 Phase diagram of $\text{YBa}_2\text{Cu}_3\text{O}_{7-x}$

In order to understand better the behavior of $\text{YBa}_2\text{Cu}_3\text{O}_{7-x}$ and to know what decomposition products can be formed in the high temperature range, phase diagrams from B.J. Lee and D.N. Lee [23] were analyzed. Figure 6.3 shows five pictures of such triangular phase diagrams with each at different temperatures, so the temperature behavior between 900°C and 1000°C is fully covered. The phase diagrams were taken in oxygen and the annealing process went on for several days so that the sample was in equilibrium.

The triangular shape of the phase diagrams is necessary, since there are three starting products involved in the preparation of $\text{YBa}_2\text{Cu}_3\text{O}_{7-x}$ samples; namely Y_2O_3 , CuO_x and BaO .

It is important to notice that the ratios of the components involved are labeled differently, so $3:1:2 = \text{YBa}_2\text{Cu}_3\text{O}_{7-x}$, $1:2:1 = \text{Y}_2\text{Ba}_1\text{Cu}_1\text{O}_5$ and so on.

From the x-ray characterization of the PAC samples it is known that in the preparation of 1-2-3 we get a small fraction of a second phase $\text{Y}_2\text{Ba}_1\text{Cu}_1\text{O}_5$, which is called 2-1-1. Hence by observing the phase diagram at 900°C it is known that we must be within the vicinity of 1-2-3.

The measurements taken at high temperature, above the decomposition temperature of $\text{YBa}_2\text{Cu}_3\text{O}_{7-x}$, show that only site B at $\nu_Q = 56$ MHz and C at $\nu_Q = 244$ MHz can still be observed. It is known from the phase diagram that these two sites can then only be $\text{Y}_2\text{Ba}_1\text{Cu}_1\text{O}_5$ and $\text{Y}_2\text{Cu}_2\text{O}_5$. In order to distinguish between this two phases, PAC measurements were done on $\text{Y}_2\text{Cu}_2\text{O}_5$, see next chapter. The result of this investigation was that one can define that:

- Site A is referring to ^{111}In in $\text{YBa}_2\text{Cu}_3\text{O}_{7-x}$
- Site B is referring to ^{111}In in $\text{Y}_2\text{Ba}_1\text{Cu}_1\text{O}_5$
- Site C is referring to ^{111}In in $\text{Y}_2\text{Cu}_2\text{O}_5$

which is in very good agreement with the literature, table 5.1 and 5.2.

With these results it is known that above the decomposition of $\text{YBa}_2\text{Cu}_3\text{O}_{7-x}$ the fix point is no longer at the connection line between 1-2-3 and 2-1-1 but dropped and is now on the solid line between 2-1-1 and the new phase $\text{Y}_2\text{Cu}_2\text{O}_5$. This

means that BaO, which is the component with the lowest melting point, had to be decomposed.

With a further increase of the temperature we know that 2-0-2 vanishes but instead we get an exponential phase, which was labeled as site D, around $v_Q = 0$ this phase refers to the liquid phase and is also indicated by the phase diagram through the tie lines. So we are able to define:

- site D as the liquid phase.

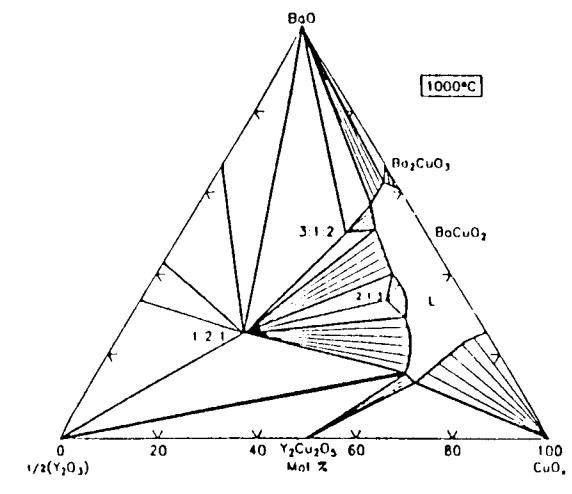
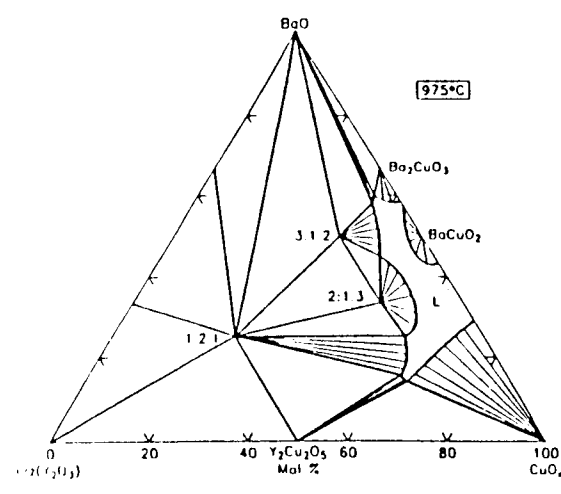
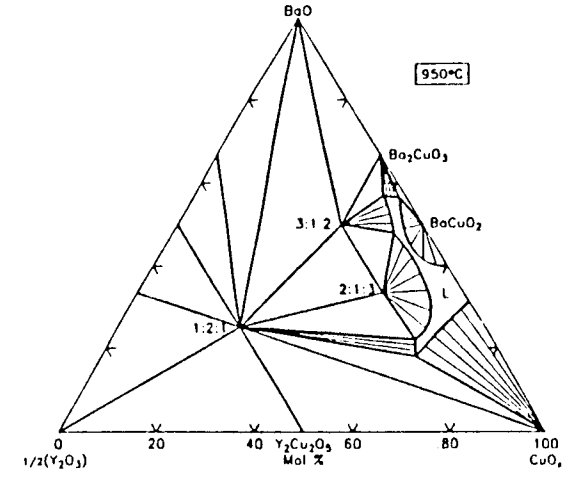
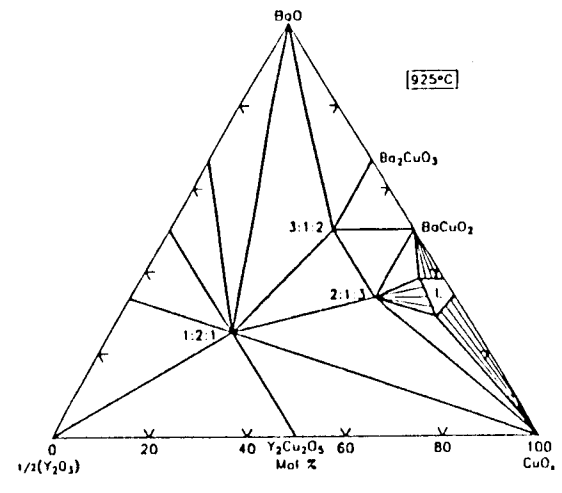
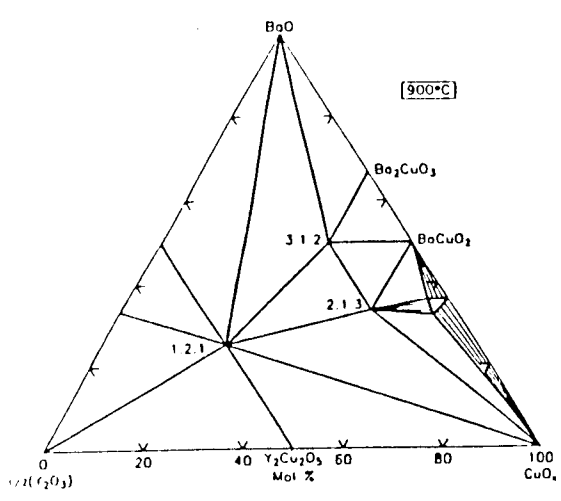
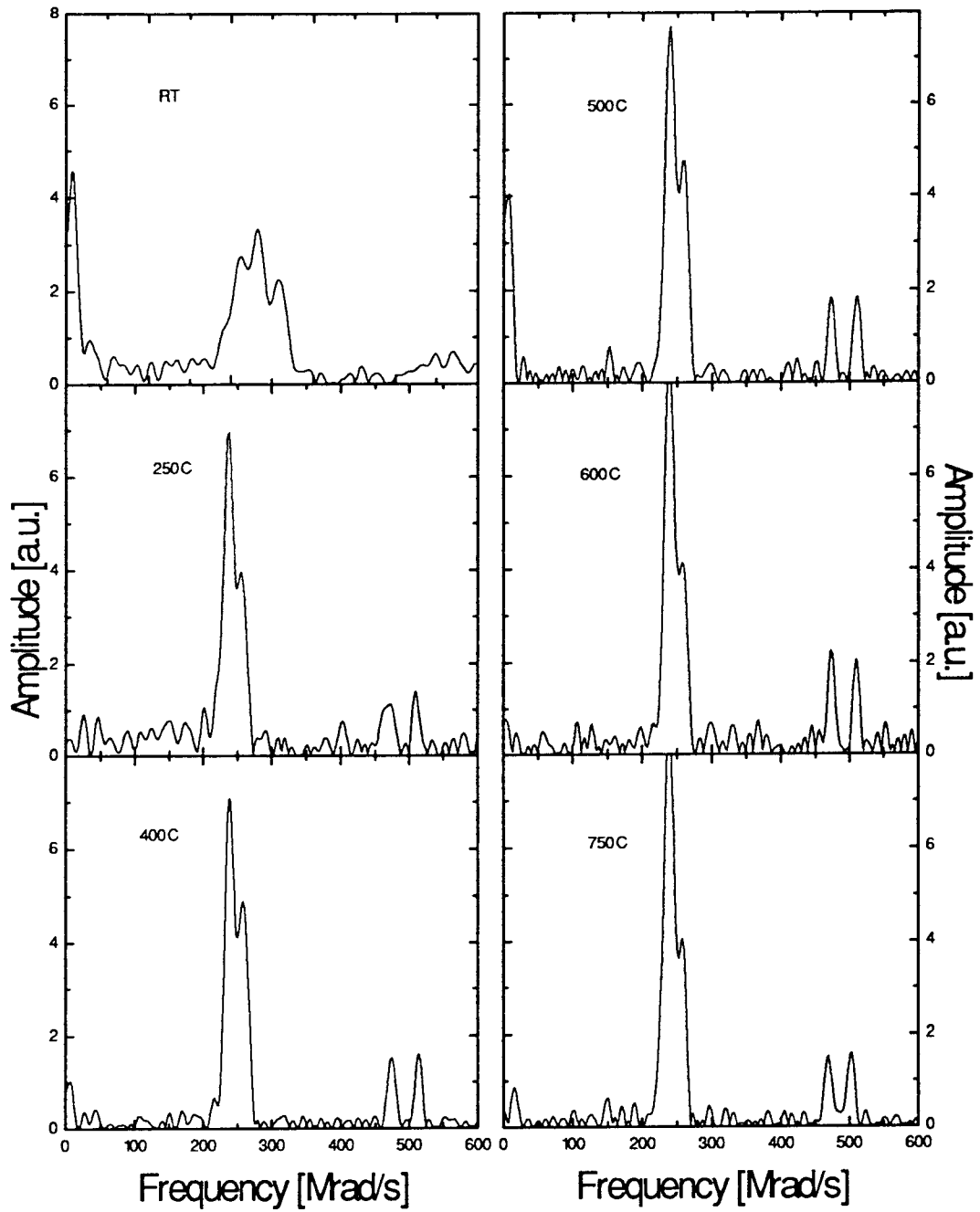


Fig. 6.3 The triangular phase diagrams of $\text{YBa}_2\text{Cu}_3\text{O}_{7-x}$ for various temperatures [23].

6.4 PAC data on $Y_2Cu_2O_5$ in flowing air

The only unknown frequency in the observed PAC measurements was due to the site C at $\nu_Q = 244$ MHz with $\nu_Q = \frac{10}{3\pi} \omega_0$. Figure 6.4 shows the results of the PAC measurements on 2-0-2 in flowing air. The new phase above 1150C next to the liquid phase is Y_2O_3 which is the second product after the destruction of $Y_2Cu_2O_5$. As can be observed the frequency for 2-0-2 is identical to the site C from chapter 6.1 and chapter 6.2. Between 250°C up to 950°C there are two sites with $\eta = 1$ and almost the same frequency, which refer probably to the two Y-sites in 2-0-2. Between 1050°C and 1150°C the fraction of $Y_2Cu_2O_5$ decreases which is in agreement with the decomposition temperature of $Y_2Cu_2O_5$. Above the decomposition temperature which occurs at 1100°C [24] a new phase can be identified as Y_2O_3 and liquid is created.

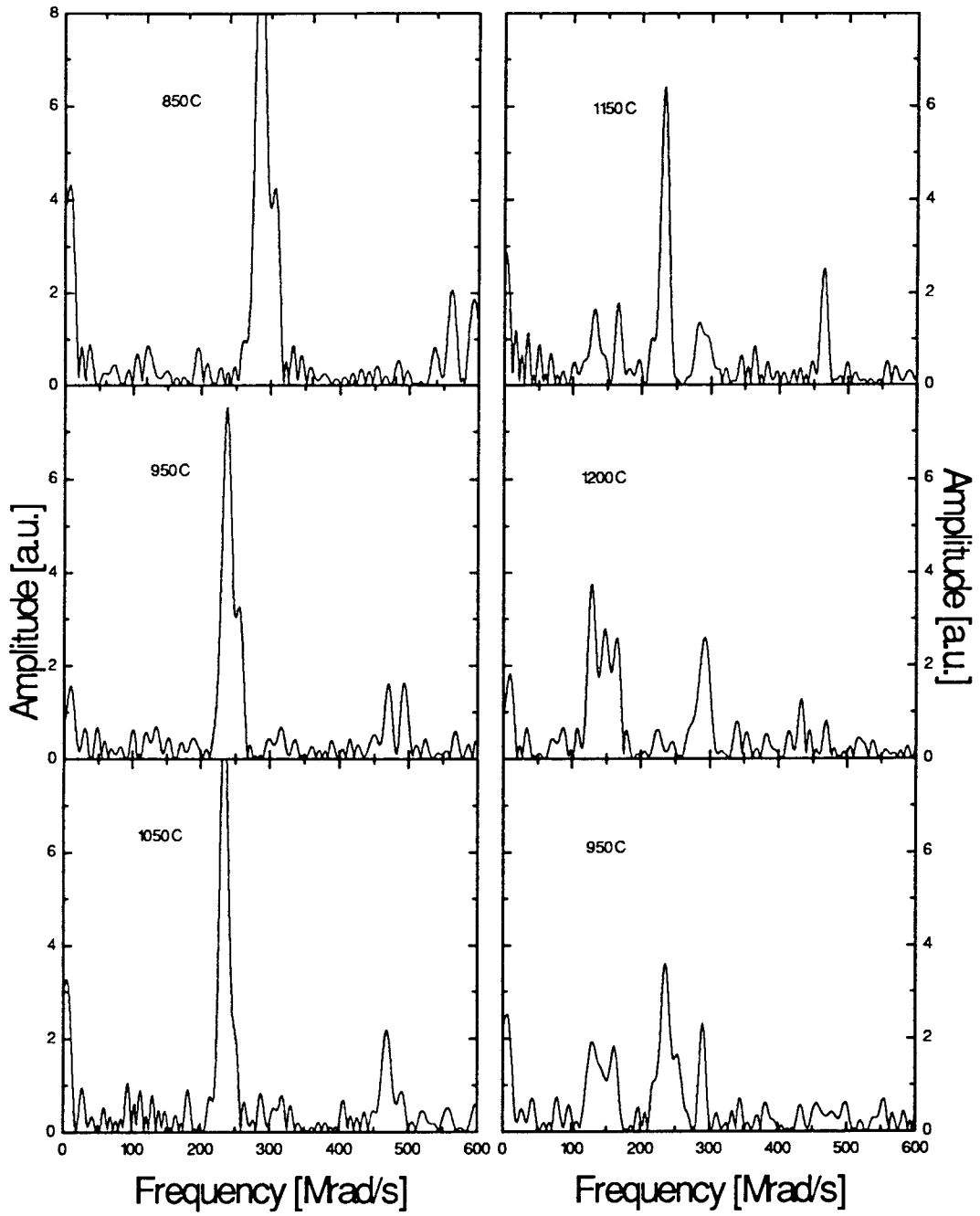
Y₂Cu₂O₅



in flowing air

Fig. 6.4 The Fourier transform of the time spectra obtained by PAC on Y₂Cu₂O₅ in flowing air at various temperature.

Y₂Cu₂O₅



cont.from Figure 6.4

in flowing air

6.5 The fitting of the observed PAC frequencies

The measured $A2G2_{(t)}$ s are the superpositions of $A2G2_{(t)}$ s resulting from probe interactions of different crystal phases. The fractions indicate the fractional weight of these phases in the total $R(t)$ -function with $\sum f_i = 1$ as was discussed in chapter 4.2. The $A2G2$ of each phase is an oscillating function of time depending on the PAC frequencies ω_1^i, ω_2^i and $\omega_3^i = \omega_1^i + \omega_2^i$. For each site a Lorentzian broadening is assumed.

The maximum number of sites used in fits was five, four static sites and one liquid site. The errors in the PAC parameters depend mainly on:

- the statistics of data accumulation, the longer the data accumulation the smaller the error bars in the $A2G2_{(t)}$ since this is a statistical method.
- the S/N ratio which is the ratio of accidental to true coincidences

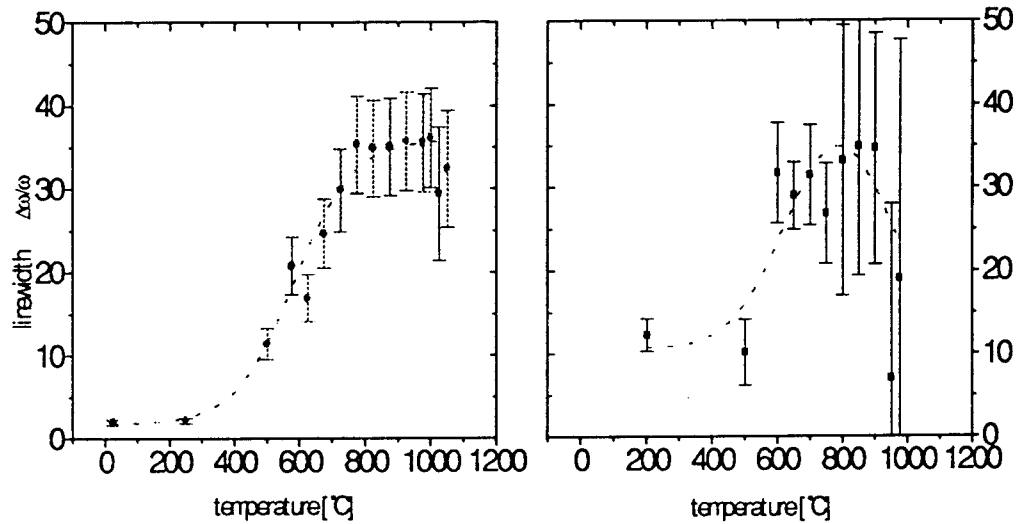
One important parameter that has to be fitted is the full line width $\frac{\Delta\omega}{\omega}$ which describes the line-broadening. Changes in the line broadening can affect the fraction and frequencies and therefore the fit as a whole. In our case we fitted $\frac{\Delta\omega}{\omega}$ in the following way:

Due to the overlapping of the frequencies from different fractions namely 1-2-3 and 2-1-1 it was not realistic to fit for both phases simultaneously. Therefore the line broadening $\frac{\Delta\omega}{\omega}$ for 2-1-1 was assumed to be zero based on previous measurements, where 2-1-1 was the only fraction. The following line broadening could be found which did not change over temperature.

$$\frac{\Delta\omega}{\omega} = 0(1.2) \% \quad \text{for } Y_2Ba_1Cu_1O_5$$

with this result the line broadening of $YBa_2Cu_3O_{7-x}$ was fitted and the behavior of $\frac{\Delta\omega}{\omega}$ versus the temperature can be seen in figure 6.5.

Fig. 6.5 The full line width for flowing oxygen on the left side and for flowing air on the right side



One can immediately see that the line width below the phase transition is much smaller than above, this shows that some dynamic interaction must be involved. Below the phase transition the values of the linewidth for flowing oxygen are smaller which can be explained due to the fact that more oxygen is available to the sample than for flowing air. While above transition the linewidth has about the same value for both cases.

7. Discussion and conclusions

7.1 Phase stability of $\text{YBa}_2\text{Cu}_3\text{O}_{7-x}$ and second phases

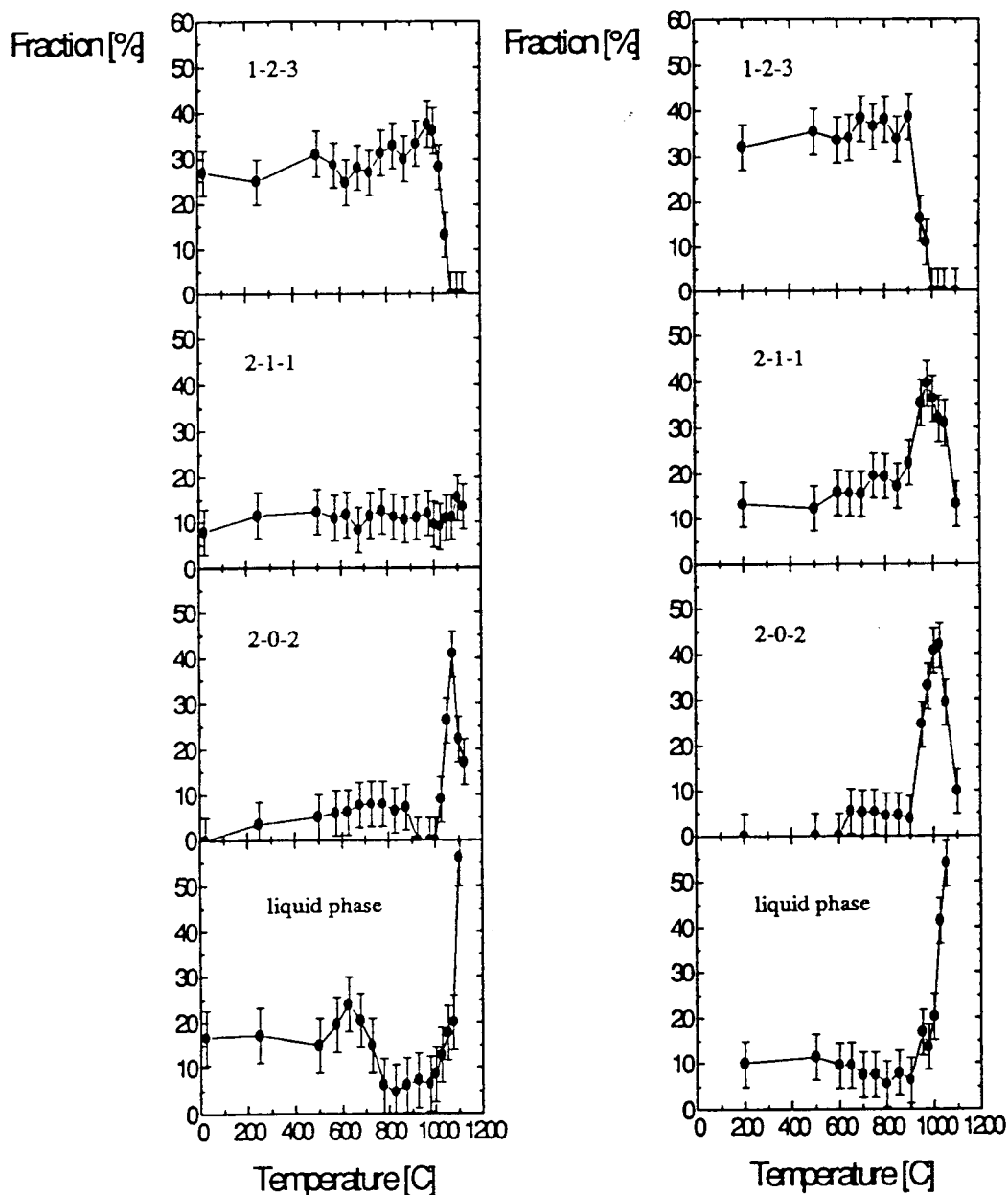
Figure 7.1 summarizes and elucidates the PAC data. It shows the fraction of all observed phases versus the temperature. With this figure one can very well see at what temperature the phases disappeared and what the decomposition products are.

To summarize chapter 6.3:

- Site A is the site in $\text{YBa}_2\text{Cu}_3\text{O}_{7-x}$ where it is possible that the ^{111}In atom is substitutional for an Y atom.
- site B is the site in $\text{Y}_2\text{Ba}_1\text{Cu}_1\text{O}_5$.
- site C refers to the PAC signal for $\text{Y}_2\text{Cu}_2\text{O}_5$.
- and site D the PAC signal for the liquid phase in the higher temperature range, where an exponential relaxation model is valid. This same model was also used as an approximation for sites at lower temperatures in dirty phases (no single phase) which had a broad frequency distribution.

Figure 7.1a.) contains the measurements in flowing oxygen and figure 7.1b.) shows the data obtained for $\text{YBa}_2\text{Cu}_3\text{O}_{7-x}$ in flowing air. From these figures one can observe the sudden disappearance of 1-2-3 at higher temperatures and the increase of the fraction of 2-0-2 and 2-1-1 at the same time.

Figure 7.1 Fraction of all observed phases 1-2-3, 2-1-1, 2-0-2 and liquid phase vs. the temperature for a.) in flowing oxygen and b.) in flowing air



By careful analysis one can see that the only difference in the data is that in flowing oxygen, $\text{YBa}_2\text{Cu}_3\text{O}_{7-x}$ has a higher decomposition temperature than in flowing air. Table 7.1 shows the beginning of the decomposition for the observed components.

It is interesting to notice that at the decomposition temperature of $\text{YBa}_2\text{Cu}_3\text{O}_{7-x}$ for flowing air both fractions 2-1-1 and 2-0-2 increase while at the decomposition temperature of 1-2-3 in flowing oxygen only the fraction of 2-0-2 rapidly increases but the fraction of 2-1-1 does not change.

Another point to notice is that in flowing oxygen $\text{YBa}_2\text{Cu}_3\text{O}_{7-x}$ decomposes over a smaller temperature range than it does for flowing air.

One can also observe that in the temperature range between 500°C - 700°C a small bump occurs for the fraction of the exponential phase in flowing oxygen. This bump is probably due to changes in the missing fraction, since no change in the identified phases can be observed. At this temperature range no liquid is possible.

Table 7.1 The observed decomposition temperatures for $\text{YBa}_2\text{Cu}_3\text{O}_{7-x}$ and related compounds

material	decomposition in air	decomposition in oxygen
$\text{YBa}_2\text{Cu}_3\text{O}_{7-x}$	900 [$^\circ\text{C}$]	1000 [$^\circ\text{C}$]
$\text{Y}_2\text{Ba}_1\text{Cu}_1\text{O}_5$	1050 [$^\circ\text{C}$]	1150 [$^\circ\text{C}$]
$\text{Y}_2\text{Cu}_2\text{O}_5$	1050 [$^\circ\text{C}$]	1100 [$^\circ\text{C}$]

At this point it is important to notice that the measured decomposition temperatures for the observed phases are lower than the temperatures reported in the literature for these phases. P. Gallagher [6] found that the decomposition temperature for 1-2-3 in flowing air would be 1015°C and in flowing oxygen 1027°C . One can suggest that the temperature difference is due to the fact that the In probes are getting mobile at these temperatures. From figure 7.1 one can observe that at the decomposition temperature of $\text{YBa}_2\text{Cu}_3\text{O}_{7-x}$ the fraction of the two phases $\text{Y}_2\text{Ba}_1\text{Cu}_1\text{O}_5$ and $\text{Y}_2\text{Cu}_2\text{O}_5$ increases very suddenly, while the fraction of the liquid phase gets very big at the decomposition temperature of $\text{Y}_2\text{Ba}_1\text{Cu}_1\text{O}_5$ and $\text{Y}_2\text{Cu}_2\text{O}_5$.

7.2 Orthorhombic - tetragonal phase transition

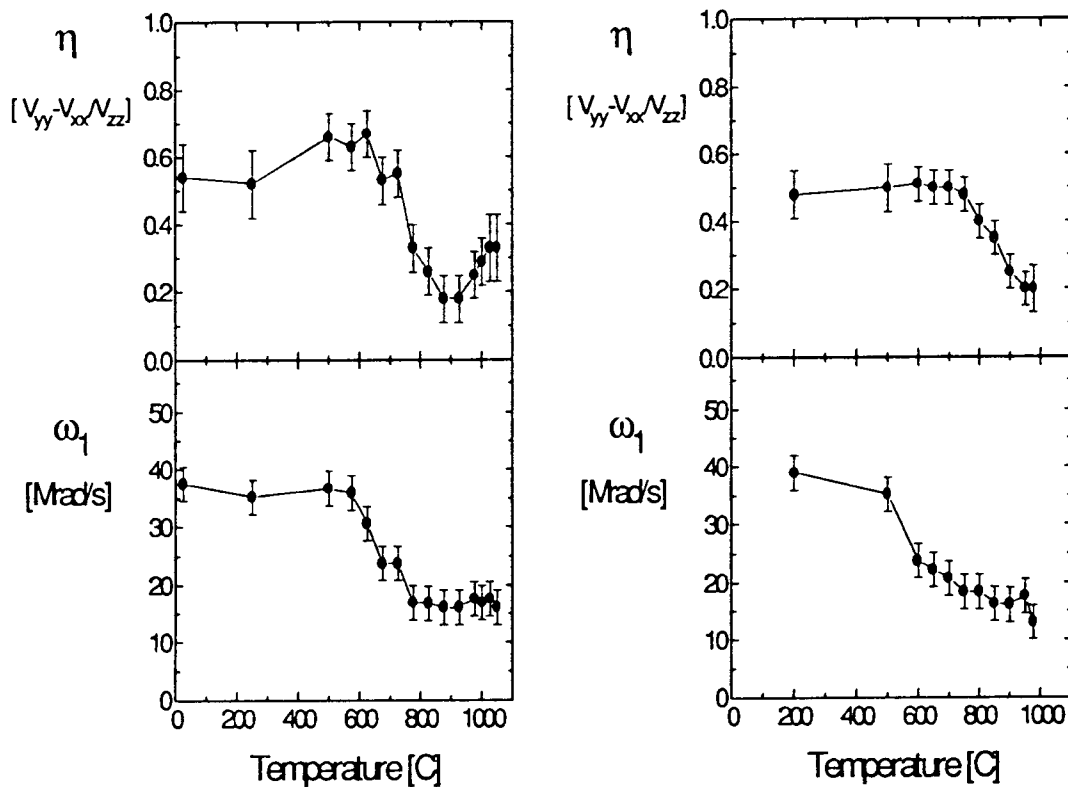
In figure 7.2 the asymmetry parameter η and the frequency ω_1 are plotted vs the temperature for the $\text{YBa}_2\text{Cu}_3\text{O}_{7-x}$ site for flowing oxygen on the left side and flowing air on the right side. From the plots for the asymmetry parameter one is able to identify the transition temperature where $\text{YBa}_2\text{Cu}_3\text{O}_{7-x}$ goes from the orthorhombic phase to the tetragonal phase. These temperatures which also agree with the neutron diffraction measurements and with datas represented by P.K. Gallagher et al. [6] given in chapter 1 are shown in table 7.2.

It also should be emphasized that the frequency for $\text{YBa}_2\text{Cu}_3\text{O}_{7-x}$ already decreases smoothly before the actual phase transition occurs.

Table 7.2 The observed orthorhombic-tetragonal phase transition temperature of YBaCuO from the PAC measurements

Transition temperature in flowing air	620 [°C]	Transition temperature in flowing oxy.	680 [°C]
--	----------	---	----------

Fig. 7.2 The asymmetry parameter η and the frequency ω_1 for YBaCuO versus the temperature for with flowing oxygen on the left side and flowing air on the right side



7.3 The inapplicability of the a-b fluctuation model

A very important aspect in this thesis was the investigation of the validity of the a-b fluctuation model, which was already explained in chapter 3.5.

Earlier PAC measurements [9] suggested this model since one seemed to observe the linewidth behaving as explained in chapter 3.5.

An increase in the line broadening was observed in the temperature range between 500°C and 800°C, right where the transition from orthorhombic to tetragonal phase should occur for $\text{YBa}_2\text{Cu}_3\text{O}_{7-x}$. The line width that was calculated by the computer changed from 6% half line width at 500°C to 18% at 800°C for flowing oxygen, and from 5% to 18% for flowing air. Above 800°C the linewidth did not change as can be seen in Fig. 6.5. This stability of the linewidth above 800°C behaves opposite to the suggested a-b fluctuation model. If it were a dynamic interaction the linewidth would become very large and then become smaller again as the temperature rises.

So it is most likely that the increase of the measured linewidth above phase transition is simply a change in the static linewidth due to lattice disorder.

The inapplicability of the a-b fluctuation model is also confirmed by H. Plank et al.[25]. Here the oxygen content of $\text{YBa}_2\text{Cu}_3\text{O}_{7-x}$ was varied by annealing the sample in air for two hours at temperatures between 530K and 1220K followed by a quench to room temperature. Afterwards the oxygen content was determined by weighing the samples after each temperature treatment. Figure 7.3 [25] shows the published data, where the frequency plot ν_Q is in good agreement with the measured data from chapter 6. However the asymmetry parameter η above 700°C behaves opposite to the observed η values which were shown in Fig.7.2. The agreement of the frequencies from Fig. 7.3 and Fig.7.2 proves that no a-b fluctuation is possible since $\text{YBa}_2\text{Cu}_3\text{O}_{7-x}$ in Fig. 7.3 was cooled back to room temperature.

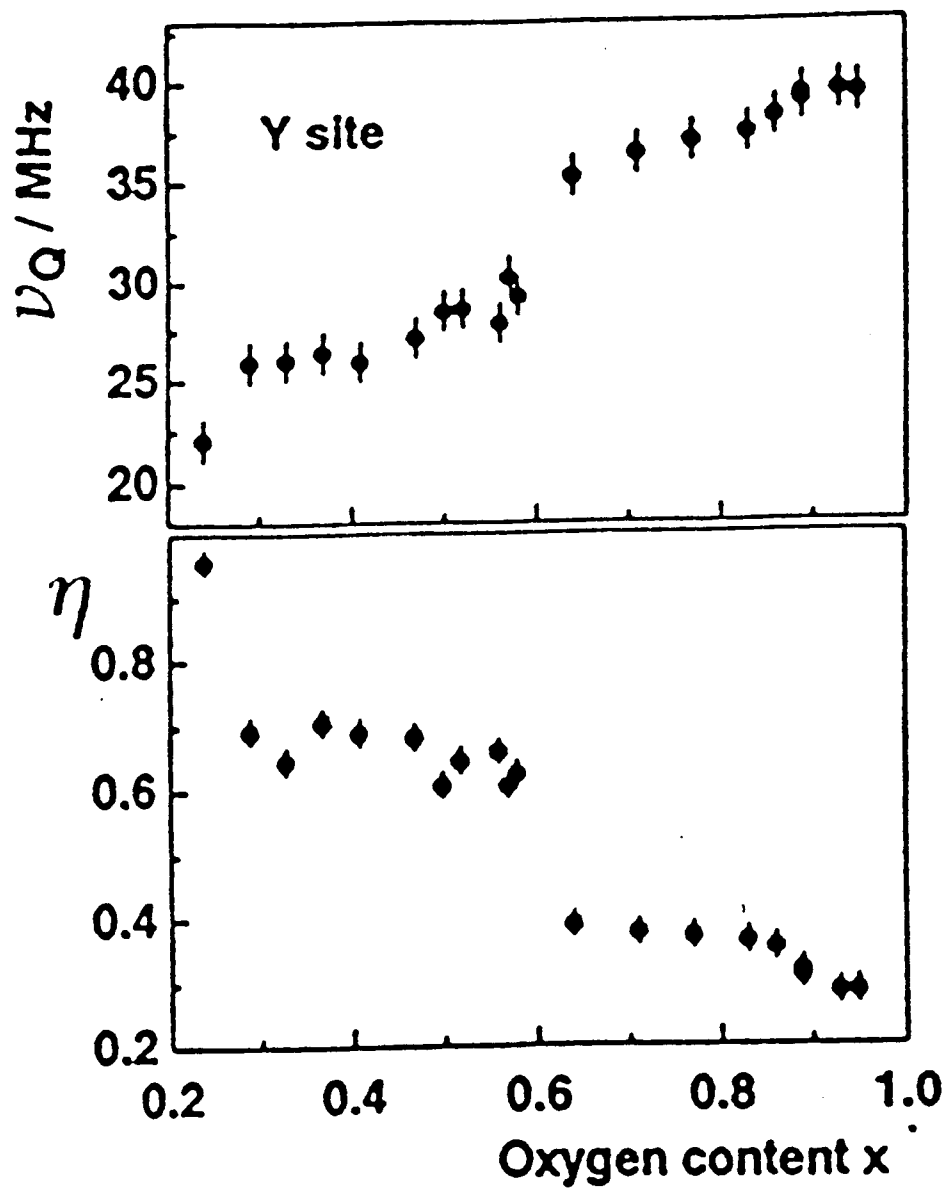


Fig. 7.3 The Quadrupole coupling constant v_Q and the asymmetry parameter η of $YBa_2Cu_3O_{7-x}$ after quenching the sample to RT. [25].

7.4 The new phases above decomposition temperature $Y_2Cu_2O_5$ and $Y_2Ba_1Cu_1O_5$

It was shown in chapter 6.4 that the site with frequencies $\nu_Q = 142$ MHz is a site in the $Y_2Cu_2O_5$ phase, and not another lattice site in 1-2-3 as has previously been claimed by A. Bartos and M. Uhrmacher [26]. Both suggested that a complicated crystal structure like $YBa_2Cu_3O_{7-x}$ could be understood as being built from some different substructures. Each substructure characterized by a typical oxygen coordination which causes a typical EFG for ^{111}Cd at the corresponding cation site. Therefore they measured the EFG of ^{111}Cd in $Y_2Cu_2O_5$, as this compound contains a fourfold oxygen coordination around the Cu-atoms which has strong similarities to the Cu1-site in $YBa_2Cu_3O_{7-x}$. Their observed PAC spectra for a $Y_2Cu_2O_5$ polycrystalline sample are very similar to the measured PAC data already shown in Fig.6.4.

But the question of whether ^{111}Cd really substitutes to the Cu atom in $Y_2Cu_2O_5$ is never answered, and there is no direct proof. A. Bartos and co. had to admit that also the Y-site can be substitutional. In our point ion charge model calculations, from chapter 5.3, which were done for both the Cu site as well as for the Y site it could be shown that the calculated η value, with $\eta = 0.9$ for Y-site is much closer to the experimental value of $\eta = 1$ than the calculated η value for the Cu site with $\eta = 0.05$. This suggests the idea that ^{111}Cd is substitutional at the Y-site but not at the Cu site and hence the frequency at $\nu_Q = 240$ MHz is not ^{111}Cd at the Cu1 site in $YBa_2Cu_3O_{7-x}$ but the frequency of the $Y_2Cu_2O_5$ phase above the decomposition temperature.

Finally it is worth mentioning that the frequency $\nu_Q = 240$ MHz first occurs in our measured data after the decomposition of $YBa_2Cu_3O_{7-x}$, which agrees with the phase diagrams in chapter 6.3. This again shows that during the process of their sample preparation or during the quenching of the sample $Y_2Cu_2O_5$ has to be created.

7.5. Summary

In this work PAC data were taken of $\text{YBa}_2\text{Cu}_3\text{O}_{7-x}$ in flowing air as well as in flowing oxygen in the high temperature range between room temperature and 1200 °C.

During the measurements one could observe a change in frequencies, line width and asymmetry parameter that had an anomaly at the orthorhombic-tetragonal phase transition, which occurs at 620°C for flowing air and at 680°C for flowing oxygen [5].

When the temperature was raised sufficiently one could observe the PAC signal for YBaCuO disappear. This happened at about 900°C in flowing air and at 1000°C for flowing oxygen, which are the expected decomposition temperatures.

Above the decomposition temperature a new site was observed at $\nu_Q = 244$ MHz. This site could be identified as $\text{Y}_2\text{Cu}_2\text{O}_5$. For a long time this site was misinterpreted as ^{111}In substitutional at a copper site in $\text{YBa}_2\text{Cu}_3\text{O}_{7-x}$.

With these data one is able to investigate the phase diagram of $\text{YBa}_2\text{Cu}_3\text{O}_{7-x}$.

Calculations of the electric field gradient for $\text{YBa}_2\text{Cu}_3\text{O}_{7-x}$ at various lattice sites were done by a point ion model. These calculations were done to see what qualitative differences there are between the EFG at different sites. The calculated asymmetry η and the electric field gradient did not agree with the experimental parameters. One can not really expect the point ion model to be correct, since the electric charges in $\text{YBa}_2\text{Cu}_3\text{O}_{7-x}$ are not localized and the distribution of the electrons in the lattice is unknown.

In order to explain apparent line width anomalies in earlier measurements a dynamic behavior was assumed which suggested the a-b fluctuation model. Here the line broadening increased and then decreased again with rising temperature. The line width, which is more accurately measured in the present work, shows no anomaly but shows a different behavior and indicates that the a-b fluctuation model does not apply for 1-2-3.

References

1. M.K. Wu et al., Phys. Rev. Lett. 58, 908 (1987)
2. J.G. Bednorz and K.A. Müller, Z. Phys. B64, 189 (1986)
3. A.W. Hewat, Phys. Scripta V.44, 38 (1991)
4. R.J. Cava et al., Physica C 165, 419 (1990)
5. E. Specht et al., Phys. Rev. B 37, 7426 (1988)
6. P.K. Gallagher, Thermochemica Acta 174, pp. 85-97 (1991)
7. G. Weidlich, J. A. Gardner and J. Sommers, unpublished
8. J. Fransaer et al., J. Appl. Phys. 65, 3277 (1989)
9. R. Schwenker, M.S. Thesis, Oregon State University (1990) unpublished
10. H. Frauenfelder and R. M. Steffen, in Alpha-Beta- and Gamma-Ray Spectroscopy Vol.2, edited by K. Siegbahn, North-Holland, Amsterdam (1965), Chap. XIXA, pp. 997-1198.
11. G. Schatz and A. Weidinger, Nukleare Festkörperphysik, B.G. Teubner Stuttgart (1992), pp. 35-43
12. W.E. Evenson et al., Hyperfine Inter. 62, 283 (1990)
13. G. Schatz and A. Weidinger, Nukleare Festkörperphysik, B.G. Teubner Stuttgart (1992), pp. 98-102
14. H. Plank, F. Meyer, W. Witthun, Phys. Lett. A133, 451 (1988)
15. M. Uhrmacher and A. Bartos, Hyperf. Inter. 61, pp. 1073-1080 (1990)

16. M. Uhrmacher et al., *J. Less.-Comm. Metals* 150, 185 (1989)
17. H. Su, Ph.D. Thesis, Oregon State University (1989), unpublished
18. A. Biblioni et al., *Phy. Rev. B* 32, 2393 (1985)
19. H. Jaeger, Ph.D. Thesis, Oregon State University (1987) unpublished
20. A. Biblioni et al., *Phys. Rev. B* 37, 4743 (1988)
21. M. Uhrmacher and A. Bartos, *Hyperf. Inter.* 61, 1097 (1990)
22. I.D. Brown, *Proceedings of the Int. Cnf. on the Chem. of Elect. Ceramic Material*, NIST Special Pub. 804, P.K. Davies and R.S. Roth, 471 (1991)
23. John D. Whitley and Robert S. Roth, *Phase Diagrams for High T_c Superconductors*, The American Ceramic Society, Fig.S-096 (1991)
24. John D. Whitley and Robert S. Roth, *Phase Diagrams for High T_c Superconductors*, The American Ceramic Society, Fig.S-038 (1991)
25. H. Plank et al., *Hyperf. Inter.* 61, 1139 (1990)
26. A. Bartos and M. Uhrmacher, *Hyperf. Inter.* 61, 1101 (1990)
27. *Handbook of Chemistry and Physics*, 66th Edition, F 164 (1985-1986)
28. C. Ambrosch-Draxl, *Physica C* 162, 1353 (1989)